JOURNAL OF GEOPHYSICAL RESEARCH, VOL. ???, XXXX, DOI:10.1002/,

Propagating modes of variability and their impact on the western boundary current in the South Atlantic

Sudip Majumder,[1,2,4] Marlos Goes,[1,2] Paulo S. Polito,[3] Rick Lumpkin,[2]

Claudia Schmid,[2] and Hosmay Lopez[1,2]

Corresponding author: Sudip Majumder, now at University of Georgia, Athens, GA, USA.

Email: sudip.majumder@uga.edu

[1]Cooperative Institute for Marine and Atmospheric Studies, University of Miami, Miami, FL, USA

[2]Atlantic Oceanographic and Meteorological Laboratory, NOAA, Miami, FL, USA.

[3]Departamento de Oceanografia Fisica, Quimica e Geologica, Sao Paulo, Brazil

[4]University of Georgia, Athens, GA, USA.

This article has been accepted for publication and undergone full peer review but has not been through the copyediting, typesetting, pagination and proofreading process which may lead to differences between this version and the Version of Record. Please cite this article as doi: 10.1029/2018JC014812

Key Points.

(i) The Complex Empirical Orthogonal modes are estimated from sea surface heights in the South Atlantic Ocean at interannual frequencies.

(ii) The Complex Empirical Orthogonal modes show Rossby wave-like propagation which influences the sea surface height in the western boundary.

(iii) The modes are connected to the recent changes in the equatorial Pacific Ocean via atmospheric teleconnections.

Abstract.

Studies have suggested that the South Atlantic Ocean plays an important role in modulating climate at global and regional scales and thus could serve as a potential predictor of extreme rainfall and temperature events globally. To understand how propagating modes of variability influence the circulation of the subtropical gyre and the southward flowing Brazil Current at interannual frequencies, a Complex Empirical Orthogonal Function (CEOF) analysis was performed on the satellite-derived sea surface height. The first three CEOF modes explain about 23%, 16% and 11% of the total interannual variability and show clear westward propagation with phase speeds comparable to that of theoretical baroclinic mode 1 Rossby waves. Results suggest that there is a change in the way energy is distributed among the modes before and after 2005. Before 2005, the sea surface height variability in the western boundary in the South Atlantic is more closely linked to the first and the second modes, while the third mode dominates after 2005. This change in energy distribution around 2005 is associated with the recent El Niño-Southern Oscillation (ENSO) regime shift in the Pacific Ocean via atmospheric teleconnections. We found that the 1st CEOF mode is strongly correlated with eastern Pacific (i.e., canonical) ENSO events and the Pacific Decadal Oscillation, whereas, the 3rd CEOF is correlated **to** central Pacific (i.e., Modoki) ENSO.

These results are useful to understand the overall dynamics of the South Atlantic and to potentially improve predictability of Meridional Overturning Circulation and monsoon pattern changes around the world.

1. Introduction

In recent years there has been a growing attention to the importance of the South Atlantic Ocean on redistribution of heat and salt meridionally and its role in modulating the long-term climate variability at regional and global scales [*Biastoch et al.*, 2009; *Lopez et al.*, 2016a]. Sea surface temperature (SST) changes in the South Atlantic have been linked to the variability of the South American monsoon system [*Nobre et al.*, 2012; *Bombardi et al.*, 2014; *Chaves and Nobre*, 2004] as well as other monsoon systems on the globe [*Lopez et al.*, 2016a]. At interannual timescales the dominant modes of variability of SST are found to be coupled to the atmospheric dynamics [*Venegas et al.*, 1997; *Palastanga et al.*, 2002]. *Hazeleger et al.* [2003] and *Haarsma et al.* [2005] suggested that the SST anomalies in the South Atlantic are induced by the Ekman transport and later modified by wind-induced mixing, and turbulent heat fluxes.

The leading coupled mode of ocean-atmospheric interannual variability in the South Atlantic is characterized by a dipole-like SST pattern associated with a monopole in the sea level pressure (SLP) anomaly **[*Venegas et al.*, 1997; *Sterl and Hazeleger*, 2003; *Rodrigues et al.*, 2015].** This mode is known as the South Atlantic Subtropical Dipole (SASD, [*Behera and Yamagata*, 2001; *Suzuki et al.*, 2004]). The SASD is characterized in its positive phase by warm SST anomalies in the south and cold anomalies in the north, which are induced by the strengthening and poleward shift of **the** South Atlantic subtropical high [*Morioka et al.*, 2011]. The position of the South Atlantic subtropical high is greatly influenced by the El Niño-Southern Oscillation [*Rodrigues et al.*, 2015].

The El Niño-Southern Oscillation (ENSO) is the dominant coupled mode of the interannual variability **globally** and is know to influence remote ocean basins through atmospheric teleconnections [e.g. *Enfield and Mayer*, 1997; *Chambers et al.*, 1999]. Despite similarities, ENSO events differ in terms of their magnitude, evolution, and location of SST anomalies in the equatorial Pacific [*Lee and McPhaden*, 2010; *Taschetto et al.*, 2014; *Fedorov et al.*, 2015; *Xie et al.*, 2015; *Lee et al.*, 2018] as well as teleconnection patterns. In the **South** Atlantic, teleconnections from the central Niño modes are found to weaken and shift the Subtropical high equatorward which triggers the negative phase of the SASD. Conversely, central La Niña events trigger the positive phase of SASD [*Rodrigues et al.*, 2015].

The teleconnection between the central Pacific and the Atlantic occurs mainly through the Pacific-South American Wave train (PSA2, e.g. *Mo and Higgins* [1998]), the third leading mode (after SASD and ENSO) of atmospheric variability in the Southern Hemisphere [*Ashok et al.*, 2007]. These modes are known to influence extreme precipitation events in South America [e.g. *Grimm*, 2003, 2004; *De Almeida et al.*, 2007].

Previous studies suggested a delayed adjustment from the ocean to the South Atlantic coupled atmospheric modes [*Sterl and Hazeleger*, 2003]. However, they are mostly silent on how these atmospheric patterns trigger the adjustment of the ocean, and how the ocean circulation affects the SST variability and provides a memory that can be used to predict interannual to decadal features and its teleconnections.

Attempts were also made to establish a statistically robust connection between the variations in the western boundary current of the South Atlantic with those in the wind stress and its curl at spectral bands of **the** Southern Annual Mode, ENSO and SASD. For example, *Schmid and Majumder* [2018] present observation-based transport estimates of the

Brazil Current (BC) in the South Atlantic Ocean and link its variability to the large scale forcing in the South Atlantic. They found significant correlations of the volume transport with the Southern Annular Mode (SAM), SASD, and the El Niño-Southern Oscillation at interannual timescales. A recent study by *Goes et al.* [2019] uses observation-based estimates of the BC and investigates how the propagation of anomalous sea surface height (SSH) in the South Atlantic can influence its variability. The present study is an extension of *Goes et al.* [2019] and *Schmid and Majumder* [2018] where we investigate the influence of SSH propagating modes to the western boundary, and explore how the regional and inter-basin **teleconnection** patterns influence the variability of the BC at interannual timescales.

The main conjecture here is that the large scale propagating modes of variability in the South Atlantic Ocean influence the dynamics of the western boundary current (i.e. the Brazil Current). This influence is physically established through the variability of the coupling mechanisms (both remote and local) at interannual timescales. To identify the propagating modes of variability a **Complex Empirical Orthogonal Function** (CEOF) analysis [**e.g. *Enfield and Mestas-Nuñez*, 1999; *Dommenget and Latif*, [illegible]; *O'Kane et al.*, 2014**] is performed on the sea surface heights. The CEOF modes are compared with the geostrophic volume transport of the BC at 22.5^{o}S and 34.5^{o}S to understand how the dynamics in the western boundary can be influenced by them. Observation-based estimates of the volume transport of the BC is calculated using XBT transects and satellite sea surface heights from 1993 to 2016. Correlations between **CEOF** modes, climate indices, SST, and global SLP fields are analyzed to understand the potential interbasin teleconnection patterns.

2. Data and Methodology

The focus of this study is in the region between 20^{o}S and 35^{o}S in the **South Atlantic** subtropical gyre. This region encompasses the energetic 'eddy-corridor' [*Garzoli and Matano*, 2011] across the South Atlantic and is bounded by the southward flowing BC in the west and northwestward flowing Benguela Current in the east. The propagating modes of variability are computed using CEOF analysis on gridded SSH data. The gridded (0.25^o × 0.25^o) weekly SSH data above the geoid is obtained from Archiving, Validation and Interpretation of Satellite Oceanographic data (AVISO) for the years 1993 to 2016 in the South Atlantic, and to understand the large scale forcing two other data sets - the global sea surface temperature (SST) and the sea level pressure (SLP) are used. *Reynolds et al.* [2007]'s SST data are obtained from the National Climatic Data Center (NCDC) and SLP data are obtained from the NCEP2 reanalysis [*Kalnay et al.*, 1996].

Our objective is to link the CEOF modes of variability (of SSH) with the variability in volume transport of the western boundary current. For this the absolute geostrophic volume transport of the BC is estimated using SSH and Expendable Bathythermograph (XBT) transects at 22.5^{o}S and 34.5^{o}S following the method described in *Goes et al.* [2019]. In short, statistical relationships are built between the dynamic height calculated from the XBT data and altimetric SSH, which are then used to infer the dynamic height and geostrophic velocity fields in time from 1993 to 2016. The geostrophic velocity is then integrated vertically and zonally to obtain the volume transport of the BC. The reconstructed geostrophic volume transport of the BC is then estimated at 22.5°S and 34°S for the period of 1993 to 2016. Details on the XBT data handling and processing can be found in *Goes et al.* [2019].

Since we are interested in the time-dependent variability, we used a wavelet decomposition [*Torrence and Compo*, 1998] methodology using a Morlet mother wavelet to bandpass the SSH, SST, SLP and the volume transport of the BC at interannual (1.25 - 7 years) periods. **In addition to that, the SSH fields are spatially smoothed to a 1×1-degree grid using a 3° half power Loess filter to further reduce the mesoscale variability.**

2.1. CEOF analysis

CEOF analysis is often used in climate studies to identify propagating modes and can be described as an Empirical Orthogonal Function (EOF) analysis of a Hilbert transformed field [*Navarra and Simoncini*, 2010; *O'Kane et al.*, 2014]. Unlike EOF analysis, where loadings (maps) and expansion coefficients (PCs) are real, CEOF analysis returns real and imaginary loadings and PCs. The real and imaginary parts of the loadings and PCs are used to obtain spatial and temporal amplitudes and phases of the CEOFs, that are the necessary components to describe a propagating wave pattern. The spatial amplitude is estimated as the square root of the squares of real and imaginary loadings, and the temporal amplitude is similarly calculated as the square root of the PC components. The spatial phase (Φ) is estimated as

$$\Phi = tan^{-1}\frac{Im(CEOF)}{R(CEOF)}, \tag{1}$$

and the temporal phase is calculated as:

$$\theta = tan^{-1}\frac{Im(PC)}{R(PC)}. \tag{2}$$

The phase information of the CEOFs is useful in understanding the propagating nature of a physical field. The phase speed of the CEOF is calculated as $c = \omega/\nabla\Phi$, where frequency ω is the temporal derivative of Φ and $\nabla\Phi$ is calculated from smoothed-spatial maps of Φ. Herein, the CEOF analysis is performed on the bandpassed (interannual and mesoscale) **spatially smoothed** SSH fields. The use of the spatial filter significantly diminishes the mesoscale signal contained in the SSH fields and **enables** us to focus on interannual frequencies. The geographical domain used for this analysis is the Atlantic region between 20°S and 35°S, between South America and Africa.

To identify the similarity between CEOF modes and westward propagating Rossby waves, zonal averages of phase speeds are computed at different latitudes and compared with the observed phase speed of theoretical baroclinic mode 1 Rossby waves at respective latitudes [*Polito and Sato*, 2015; *Chelton et al.*, 2011]. Their phase speed is estimated as : $C_p = -\beta R^2$, where $\beta = df/dy$, f is the Coriolis parameter, and R is the mode 1 baroclinic Rossby radius of deformation.

To understand the importance of the CEOF modes for the overall dynamics in the South Atlantic, SSH fields are reconstructed using individual modes and a combination of them as

$$SSHA(x, y, t) = \sum_{m=1}^{N} W_m(t) F_m^*(x, y) \tag{3}$$

The real part of the left hand side of (3) is the reconstruction of $SSHA$ for N modes. $W_m(t)$ and $F_m(x, y)$ are the coefficient of expansion and loadings for the m^{th} mode respectively. The asterisk indicates the complex conjugate.

The evolution in time of the CEOF mode can be retrieved by multiplying $F_m(x, y)$ by a rotation matrix whose argument may vary from 0-360°. If the temporal phase $W_m(t)$ is also rotated by the same angle, the SSH reconstruction of the rotated CEOF will remain the same as equation (3).

3. Results

The SSH fields are decomposed in time into the mesoscale (28 -168 days), semiannual (168 - 456 days) and interannual (1.25 to 7 years) components using a wavelet bandpass filter. The standard deviation of the bandpassed SSH at all frequencies (Fig 1) reveals one main zonal band with values as large as 5 cm. At interannual and mesoscale periods (Fig 1a,e) this band splits into two branches west of 30°W (Fig 1), probably due to the local bathymetric influence of the Rio Grande Rise. This band is mostly constrained south of 25°S and explains approximately 30 - 40% of the total variance in this region. Two meridional bands near the western boundary can be identified at the mesoscale frequencies, one along the continental shelf probably linked with the coastally trapped waves and another further offshore with amplitude up to 10 cm (about 70% of the explained variance) linked to the eddy corridor along the BC. However, they are not prominent at interannual frequencies. At semiannual frequencies, a zonal band with large values can be seen east of 35°W between 25°S and 35°S (Fig 1c). The semiannual band does not seem to explain the variability of the SSH near the western boundary (west of 35°S along the Brazilian coast, Fig 1d).

To understand the time evolution at interannual frequencies, SSH fields are further decomposed into 1.25 - 3 years and 3 - 7 years bands and are examined in longitude-time (Hovmöller) plots along 22.5°S, 30°S and 34.5°S (Fig 2). Consistent with Fig 1, SSH at 34.5°S and 30°S exhibits larger amplitudes compared to those at 22.5°S. The Hovmöller plots for the SSH bandpassed between 1.25 - 3 years reveal relatively fine scale anomalies than that for 3 - 7 years. As expected, SSH in both the bands exhibits negative slopes and therefore suggests a westward propagation, with faster propagation speeds at 22.5°S. One interesting observation, particularly at 30°S in the 3 - 7 years band, is that the anomalies before about 2005 are stronger than after 2005. On the other hand anomalies in the 1.25 - 3 years band are slightly increased after 2005.

At both frequencies, the anomalies seem to be influenced by the local topography at 34°S (Fig 2). This can be observed (particularly at 34°S, Fig 2g) by the large amplitudes in the middle of the basin (30°W to 10°W), which is the approximate location of the Mid-Atlantic ridge.

3.1. CEOF analysis

To understand the dominant large scale patterns that represent the dynamics of the South Atlantic, CEOF maps and associated expansion coefficients (PCs) are analyzed. In the following, the details of the spatial and temporal evolution of the first three CEOF modes are described.

3.1.1. CEOF1

The CEOF mode 1 (CEOF1) explains 22.7% of the observed interannual variability of SSH (Fig 3, a,b,c). The CEOF1 real and imaginary maps represent two snapshots of this propagating signal at a 90 degree shift. CEOF1 resembles a basin-wide zonal mode, with the strongest propagating signals between 25°S and 33°S, originated in the south-east side of the basin (Cape Basin). The existence of this pattern has been shown previously using standard EOF decomposition [*Grodsky and Carton*, 2006]. The **rectified wavelet power spectrum [*Liu et al.*, 2007]** of the PC1 suggests a mean periodicity of approximately 5.5-years (Fig 4). The temporal phase (shown by dotted gray lines in

Fig 3c), varying between -180° to +180°, confirms the mean periodicity of 5.5 years. We show that the first half (0° to 180°) cycle of the reconstructed SSH using CEOF1 (Fig 5, left column) exhibits a westward propagation. The spatial phase of CEOF1 (Fig 6b) varies between 0 and 360°, showing a phase progression in the same latitude band with the velocities (arrows) indicating westward propagation. Similar to the real and imaginary maps, amplitude of CEOF1 (Fig 6a) reveals a zonal band of large values that extends from eastern side of the basin to the west. These features resemble the standard deviation map of SSH in Fig 1, and the SSH (3 - 7 years) Hovmöller plot in Fig 2, specifically at 30°S, where SSH exhibits a negative slope suggesting a basin-wide scale westward propagation.

Real and imaginary parts of PC1 (Fig 3c) show large amplitudes in years 1993 to 2005 and a decrease in amplitude from 2005 onwards. By construction the real and imaginary PCs are phase lagged by 90°, as can be seen in the time series plot (Fig 3c).

3.1.2. CEOF2

With a large amplitude south of 22°S, CEOF2 resembles a zonal mode, that explains 16.4% of the total interannual variability of the SSH (Fig 3d,e). Real and imaginary maps (Fig 3d,e) of this mode suggest a dipole like structure between 40°W and 15°W, 27°S and [illegible] CEOF2 has low energy east of 10°W and seems to be generated at about 16°W. Similar to CEOF1, the reconstructed SSH using CEOF2 (Fig 5, middle column) exhibits a westward propagation.

The temporal phase (Fig 3f) as well as the wavelet spectrum of PCs of CEOF2 (Fig 4) suggest a dominance of a 3.3 year period. The PCs show a more regular oscillatory variability before 2005, which is strongly reduced from 2005 to 2011, and thereafter, becomes more erratic. Amplitude maps of CEOF2 (Fig 6c) clearly exhibit a zonal route south of 30°S and a northwestward route that reaches 22°S. The local bathymetric feature Rio Grande Rise (centered around 29°S, 33°W) appears to modulate this mode in its westward propagation near 30°S (Fig 6c, Fig 7e), generating a dipole-like feature across this latitude (Fig 5, second column). The corresponding phase of CEOF2 (Fig 6d) reveals these westward propagating routes as can be identified in the real and imaginary maps (Fig 3d,e).

3.1.3. CEOF3

CEOF3 explains 11.3% of the interannual variability (Fig 3g,h,i). Real and imaginary maps of CEOF3 suggest two energy bands: 1) a westward zonal propagation south of 30°S across the whole basin with a wavelength of about half of the width of the basin, and, 2) a northwestward band with relatively large energies between 22°S and 30°S west of 15°W (Fig 3g). These patterns propagate westward and can be seen clearly in Fig 5 (rightmost column). The first band propagates westward while the second one propagates northwestward. Both seem to originate near (or in) the Cape Basin.

Similar to CEOF2, CEOF3 contains higher frequency variability than CEOF1. Spectral analysis of PC3 suggests that CEOF3 has a mean periodicity of about 2.5 years (Fig 4). In contrast with PC1 and PC2, PC3 has larger amplitudes from 2005 onwards. This suggests that there may be a transfer of energy among the modes at interannual timescales. This issue is further explored in section 3.2.

3.1.4. Reconstruction of SSH using CEOFs

The reconstructed SSH using the first three individual CEOF modes are shown in the Hovmöller plots for 34°S, 30°S and 22.5°S (Fig 7) with their corresponding bathymetry.

At 34°S, mode 1 between 10°W and 5°E from 1993 to 2005 shows a predominantly barotropic signal that cannot pass the topographic barrier. At this same latitude, mode 2 has a slope compatible with 1st **baroclinic** mode [*Polito and Liu*, 2003], is damped over parts of the Mid Atlantic Ridge and suggests an energy transfer between barotropic and 1st baroclinic modes over steep topography [*Barnier*, 1988]. In contrast to this, mode 3 has larger amplitudes in 10°W and 5°E during the period between 2005 and 2016, when mode 1 and 2 have small amplitudes. The year 2005 seems to mark a regime transition between modes 1 and 3, low frequency to high frequency.

At 30°S, the reconstructed SSH for the 1st mode shows a prominent basin scale westward propagation. The reconstructions using the second and the third modes exhibit more energy east of the Rio Grande Rise. At all latitudes local topography seems to play some role in modulating the modes. **This is consistent with a similar observational study by *Maharaj et al.* [2005]. They investigated SSH anomalies in the South Atlantic Ocean and identified strong westward propagation. In the presence of local topographic features, the anomalies were found significantly modulated.**
At 22.5°S no clear propagation pattern can be observed in the Hovmöller diagram, possibly due to faster speeds or shorter spatial scales, which can be aliased by the temporal filtering applied in the SSH data. The Hovmöller diagram for CEOF1 shows a damping in variability after 2005 and a simultaneous increase in CEOF3 reconstruction for the same period. This agrees well with the PC time series shown in Fig 3.

To better understand the CEOF modes and whether they are consistent with westward propagating Rossby waves in the South Atlantic, average phase speed between 35°S and 30°S is calculated for the first three modes and compared with the theoretical phase speed of the baroclinic mode1 Rossby wave (Fig 8). Phase speeds of all the modes north of 26°S have comparable magnitudes with that of the baroclinic mode 1 Rossby waves. **This result is consistent with *Maharaj et al.* [2009], who analyzed SSH anomalies in the South Pacific Ocean.** South of 26°S, in the eddy corridor [*Garzoli and Matano*, 2011] phase speeds of the modes are larger than the theoretical values. This could be an artifact of the methodology applied (filtering and the averaging of phase speeds across the basin), as well as interaction with the background flow. In addition to that, with respect to the linear theory, there is an average bias of about 25% toward high speeds, poleward of 30°S in the three basins [*Polito and Liu*, 2003].

3.2. Local and Remote forcing

As discussed above, the PCs in Fig 3 suggest that even though the mean period of variability of each mode remains mostly constant, their amplitudes vary significantly (Fig 2) over time. Particularly, it appears that before 2005, PC1 exhibits a stronger amplitude, and after 2005, PC3 increases its energy. This could be associated with changes in large scale forcing. In this section, we explore the large-scale physical processes that can excite the CEOF modes, and investigate the possibility of interocean teleconnection patterns. To accomplish this, instantaneous point-wise correlations between PCs and the gridded fields of SLP and SST are calculated (Fig 9).

Within the South Atlantic the correlation map of PC1 and SLP shows large, significant values (r∼.6) between 25°W-0, 15°S - 40°S (Fig 9g). This suggests that the SSH anomalies that propagate from the eastern side of the basin are triggered by intensification of the South Atlantic Subtropical High (SASH). The SASH is the dominant atmospheric circulation feature in the South Atlantic. According to *Morioka et al.* [2011], an anomalous southward migration and strengthening of the subtropical high causes a positive latent heat flux anomaly, leading to an anomalous shoaling of the mixed layer and subsequent warming of a thinner mixed layer from shortwave radiation, generating a positive SST anomaly. From the correlation map between PC1 and SST (Fig 9d), SST anomalies follow those of SSH between 24°S and 35°S, in that positive SSH anomalies are linked to positive SST anomalies and vice-versa. This can clearly be seen in supplementary Fig.S1. Although the generation of these SST anomalies may not be in disagreement with *Morioka et al.* [2011]'s mechanism, our results suggest that the ocean advection associated with the zonal propagation of CEOF1 drives the SST and the upper ocean heat content (supplementary **Fig S1**), and this mode can provide predictability of westward propagation of ocean heat content in this latitudinal band at longer timescales (3-7 years). *Grodsky and Carton* [2006] also pointed out that the main interannual SSH EOF mode in the South Atlantic was associated with zonal dipole-like SST anomalies.

In terms of remote influence, the SLP anomalies in the South Atlantic associated to CEOF1 seem to be a part of an atmospheric Rossby wave train emanating from the Indo-Pacific basin [*Lopez et al.*, 2016b], and extending to the Southern Indian Ocean. Indeed, the correlation map for SST (Fig 9d) shows statistically significant anomalies along the central-eastern equatorial Pacific, and a horseshoe pattern that extends from the west Pacific to south- and northeastward. This pattern is similar to the one previously defined for both Niño34 and the Pacific Decadal Oscillation (PDO) in the tropical Pacific events

[*Kao and Yu*, 2009; *Deser et al.*, 2010]. To verify this potential relationship with the Niño modes, the correlation between PC1 and several Niño indices is estimated (Figure 10, Table 1). PC1 shows good correlation (∼0.5) with Niño34 and with the PDO index (∼0.6). Although there is good indication of the link between the CEOF1 and teleconnections with the central-eastern Pacific, **these correlations do not show strong statistical significance when the number of degrees of freedom are corrected for the autocorrelation [*Bretherton et al.*, 1999].**

CEOF2 is associated with bipolar SLP anomalies in the South Atlantic (Fig 9h), and strong positive SST correlations (> 0.6) in the subtropical gyre between 10°S and 35°S (Fig 9e). The SST correlation pattern hints to the relationship between CEOF2 and the subtropical gyre strength, and potentially to coupling with the tropical Atlantic cold tongue variability. For CEOF2, no defined SLP and SST teleconnection patterns (Fig 9e,h) can be identified. This is confirmed by the small correlations (< 0.3) with Niño indices shown in Table 1. This suggests that this mode is probably driven by local wind variability in the South and Tropical Atlantic Ocean. However, this mode shows some correlation with the PSA2 index (Table 1).

The CEOF3 correlation maps also show a bipolar SLP structure in the South Atlantic, that could be associated with north-south migrations of the SASH. Its positive phase is associated with positive SST anomalies in the western South Atlantic region (25°S-35°S, *Doyle and Barros* [2002]), and with the opposite sign north of it, resembling a north-south SST dipole. This mode, similar to CEOF1, is associated with large scale SLP and SST patterns in the equatorial Pacific, and a connection to the South Atlantic SLP via atmospheric Rossby wave trains. However, the anomalies shown in CEOF3 are located mostly in the west-central equatorial Pacific, suggesting a connection to central Niño events. Central Pacific (CP) El Niño events are typically described by Niño4 index (160°E - 150°W, 5°S -5°N), the Modoki index (EMI, [*Ashok et al.*, 2007]) and the Trans-Niño (TNI) indices. The Trans-Niño index (TNI, *Trenberth and Stepaniak* [2001]) is the difference of normalized SST anomalies between the eastern (Niño3) and the central Pacific (Niño4) regions, and can be considered orthogonal to Niño3.4. Statistically significant correlations (95%) of 0.67 to 0.70 are found between PC3 and the EMI and TNI indices (Table 1).

The time series of the SLP and SST in the equatorial Pacific show strong correlations with PC1 (Fig 9j,m) and PC3 (Fig 9l,o). PC1 shows stronger correlation (95%) with PDO events (Fig 10a). Conversely, PC3 shows a strengthening after 2005 and exhibits strong correlation with the central Pacific (EP) Niño indices (EMI and TNI, Fig 10b,d). This may indicate that the teleconnections from the Pacific have changed due to the recent shift to a more positive PDO [*Burgman et al.*, 2017]. The CP region includes a good portion of the western Pacific warm pool, which by many studies (e.g *Cravatte et al.* [2009]) is in a warming phase for the last few decades, such that there has been more CP, Modoki-like [*Ashok et al.*, 2007] and western Pacific events than the classical EP events [*McPhaden et al.*, 2011; *Yu et al.*, 2017; *Liu et al.*, 2017]. This regime shift in the ENSO events, in the beginning of the 21st century [*McPhaden et al.*, 2011], is attributed to changes in the mean state of wind pattern and the thermocline depth along the equatorial Pacific, as well as to the phase change of Atlantic multidecadal Oscillation [*Yu et al.*, 2015]. These changes in ENSO regime are, however, debatable due to the limited observational record [*Lean and Rind*, 2008; *Timmermann et al.*, 2018].

So far we have examined the characteristics of the CEOF modes and investigated their response to the local and remote forcing. In the following section we explore the importance of the CEOFs to the transport variability of the Brazil Current.

3.2.1. The BC and its variability

One of the key objectives of this paper is to link the propagating modes to the dynamics in the western boundary, and then to understand how they modulate the BC. As a first step, we determine the relative importance of individual modes near the western boundary (Fig 11a, box A, B) and estimate the volume transport of the BC across two different latitudes 22.5°S and 34.5°S enclosed by A and B, using XBT transects and satellite altimetry, as described in the data and methodology section. The region enclosing 22.5°S (Fig 11a, box A) shows that the 2nd and the 3rd modes have relatively large amplitudes (Fig 5), that can give rise to strong zonal gradients translating into a significantly large transport. At 34°S (Fig 11a, box B), all the first three modes exhibit large amplitudes and strong zonal gradients. To get more insight on the relative importance of the individual modes in areas A and B, variance explained by each mode as a fraction of the total variance of the SSH is estimated. In box A (enclosing 22.5°S), CEOF2 and CEOF3 explain 37% and [illegible] the total variability, whereas at 34.5°S, CEOF1 and CEOF2 explain about 24% and 22%, and CEOF3 accounts for the 11% of the total variability. A combination of the first 6 modes can explain about 80% and 70% of the total interannual variability in boxes A and B respectively.

The daily synthetic time series (Fig 12a,b) of the volume transport of the BC at 22.5°S and 34.5°S yield mean values of 4±1.5Sv and 15±6Sv. Relatively high volume transport at 34.5°S is due to the fact that, compared to the northern latitudes (e.g. 22.5°S), BC extends to the deeper layers due to central and intermediate contributions from the subtropical gyre. The transport of the BC is bandpassed at interannual frequencies and compared with the PCs (Fig 12c,d). At 22.5°S, where the second and the third modes explain maximum interannual variability, the BC shows stronger correlation (∼0.6) with PC2 before 2005, but after 2005 it is PC3 that correlates better with the BC (Fig 12c). At 34.5°S, PC1 (before 2005) and PC3 (after 2005) exhibit good correlation (∼0.6) with the volume transport. Therefore, once can conclude that the SSH gradients (analogous to the volume transport of the BC) in the western boundary are influenced more by CEOF3 after 2005, and before 2005, it is the first two CEOF modes that are important. This result also suggests that there is a redistribution of energy among the modes before and after 2005. Because CEOF3 has strong significant correlations with the central and western Pacific ENSO indices, this suggests that the recent ENSO regime shift contributed to changes in the western boundary of the South Atlantic Ocean through atmospheric teleconnections.

4. Discussion

This study focuses on understanding the dominant propagating modes of variability in the South Atlantic and investigates the physical mechanisms, both local and remote, that influence them on interannual time scales. **To our knowledge, this is the first observation-based study to employ a complex EOF analysis to understand the main propagation modes in the South Atlantic and to explore their importance to the interannual variability of the BC.** In addition, it explores the relationship between the modes and the variability in the western boundary. The first three propagating modes, estimated from SSH between 1993 and 2016 at interannual frequencies, explain about 23%, 16% and 11% of the total variability. The first mode represents a basin-wide zonal westward propagation with a period of about 5 years. The other two modes also exhibit westward propagation, but have relatively high phase speeds and short length scales than CEOF1. CEOF2 and CEOF3 exhibit relatively complex spatial structures. CEOF2 resembles a dipole like structure south of 26°S that propagates westward in about 3 - 4 years. CEOF3 has two distinct bands characterized by large energies south of 30°S and between 22.5°S and 27°S west of 15°W.

The CEOF modes have relatively constant phase speeds as a function of latitude, close to that of the theoretical Rossby wave speeds north of about 25°S but faster than Rossby waves in the eddy corridor (between 26°S and 34°S) [*Garzoli and Matano*, 2011], where the modes exhibit relatively large speeds, due to the interaction with background flow (about 2 cm/sec northwestward, *Majumder and Schmid* [2018]). Another factor that could potentially add biases to the phase speeds is the filtering that is used to separate the interannual band.

CEOF1 shows strong correlation with the SLP in 25°W-0°, 15°S-40°S, suggesting that the modulations in the strength of the SASH excites Rossby-like features from the eastern side of the basin, which then propagates to the west in about 5 years. CEOF1 also accounts for the westward advection of the heat anomalies that contributes to the heat content and can contribute to the heat transport meridionally.

Volume transports of the BC at 22.5°S and 34.5°S are greatly modulated by the westward propagating Rossby-like features represented by the CEOF modes. When they reach the western boundary, the anomalies represented by the CEOF modes modulate the local SSH dynamics and can give rise to large gradients of SSH and thus, via geostrophy, the BC transport. **A similar interaction of Rosbby-like waves with the the East**

Australian Current is reported by *Holbrook et al.* [2011] in the South Pacific Ocean.

The interannual variability of the BC at the two locations shows that before 2005 modes 1 and 2 were more correlated to the BC at 34.5°S and 22.5°S, and after 2005 both latitudes shows stronger correlation with CEOF3. Concurrent amplitude modulations are observed among the CEOF modes, in which, before 2005, the first two modes account for the maximum variability of the SSH; after 2005, the third mode becomes more important. This redistribution of energy could be associated with changes in remote teleconnections from the tropical Pacific to the South Atlantic through mechanisms such as the Pacific-South American (PSA) wave trains. The correlation maps suggest that the CEOF1 is influenced by PDO events [*Lopez et al.*, 2016b] and CEOF3 is influenced by CP ENSO events [*Rodrigues et al.*, 2015].

Based on the spectral analysis of ENSO events, previous studies have suggested that there exist two dominant bands of ENSO variability, a lowfrequency (3-7 year) band and a quasi-biennial (∼2 years) band [e.g. *Jiang et al.*, 1995; *Wang and Wang*, 1996]. The CP events seen in the recent years are mostly quasi-biennial type, whereas the EP events are mostly associated with the low-frequency band (e.g. *Kao and Yu* [2009]; *Yu and Kim* [2010]). Temporal frequencies of CEOF1 (∼5 years) and CEOF3(∼2.5 years) and their good correlations with the EP and the non EP (Modoki like) events are therefore consistent with the spectral distribution of the ENSO events.

Wind-excited oceanic Rossby waves in the Pacific and in the North Atlantic Oceans are known to have strong influence on the western boundary currents - the Kuroshio [e.g. *Sasaki et al.*, 2013], **the East Australian Current [e.g. *Holbrook et al.*, 2011]**, and the Gulf Stream [e.g. *Osychny*, 2006]. Similar to this study, after its generation, the westward propagating Rossby waves in these ocean basins modulate the strength and the position of the northern hemisphere western boundary currents as well as the local SST dynamics in about 3-7 years. ENSO-induced and low-frequency changes in the Indian and the Pacific Oceans, are also found to significantly modulate the air-sea interaction and the underlying oceanic dynamics in these basins [*Kwon and Deser*, 2007].

Changes in the variability in the tropical Pacific have received increased attention in the past decade. Observations show that ENSO has changed its amplitude on interannual and interdecadal time scales, which affects its global teleconnections [*Xie et al.*, 2010; *Li et al.*, 2011; *Chowdary et al.*, 2012]. Due to its chaotic nature, and the low signal-to-noise ratio, ENSO events present a challenge for its predictability [*Ogata et al.*, 2013; *Wittenberg et al.*, 2014]. Due to the short length of the time series analyzed here, the detection of the changes in the Pacific teleconnections and relationships to the CEOF modes are borderline statistically significant. This problem could be overcome by using coupled model simulations **[e.g. *O'Kane et al.*, 2014]**, which is beyond the scope of this paper.

The teleconnection between the South Atlantic and PDO has been previously shown at interannual to decadal timescales with SSH and SST anomalies, and may be used as a proxy for the AMOC variability [*Lopez et al.*, 2016b], and can also influence the circulations and precipitation anomalies over South America [*Mo and Paegle*, 2001; *Carvalho et al.*, 2004] and North America [*Delworth et al.*, 2015]. CEOF1 shows strong correlation to SST patterns across the South Atlantic and may indeed represent the main conduit for Ocean Heat Content anomalies. This relationship with Ocean Heat Content can provide a multi-year predictability for AMOC, Brazil Current and coastal sea level. The observed decrease in SSH variability in a 3-7 year timescale can be explained by the decrease in amplitude of this mode after 2005.

It is noted that the CEOF analysis assumes the analysed dynamics are linear and stationary and is not suitable for dispersive processes. For non dispersive processes occurring in a narrow frequency band, the CEOFs are a fairly robust method [*Merrifield and Guza*, 1990]. However, one should be careful in interpreting the spatial patterns of the CEOFs.

Acknowledgments. Authors (SM and MG) acknowledge funding (grant number 1537769) from National Science Foundation and support from Atlantic Oceanographic and Meteorological Laboratory of the National Oceanic and Atmospheric Administration (NOAA). HL acknowledges funding from NOAA Climate Program Office its CVP program (GC16-208). This research was also carried out in part under the auspices of the Cooperative Institute for Marine and Atmospheric Studies (CIMAS), a cooperative institute of the University of Miami and the National Oceanic and Atmospheric Administration (NOAA), cooperative agreement NA10OAR432013. Altimeter products were produced by Ssalto/Duacs and distributed by AVISO, with support from *Cnes* (http://www.aviso.altimetry.fr/ducas/).

References

Ashok, K., S. K. Behera, S. A. Rao, H. Weng, and T. Yamagata (2007), El Niño Modoki and its possible teleconnection, *Journal of Geophysical Research: Oceans*, *112*(C11).

Barnier, B. (1988), A numerical study on the influence of the Mid-Atlantic Ridge on nonlinear first-mode baroclinic Rossby waves generated by seasonal winds, *Journal of*

Physical Oceanography, *18*(3), 417–433.

Behera, S. K., and T. Yamagata (2001), Subtropical SST dipole events in the Southern Indian Ocean, *Geophysical Research Letters*, *28*(2), 327–330.

Biastoch, A., C. W. Böning, F. U. Schwarzkopf, and J. Lutjeharms (2009), Increase in Agulhas leakage due to poleward shift of Southern Hemisphere westerlies, *Nature*, *462*(7272), 495.

Bombardi, R. J., L. M. Carvalho, C. Jones, and M. S. Reboita (2014), Precipitation over eastern South America and the South Atlantic sea surface temperature during neutral ENSO periods, *Climate dynamics*, *42*(5-6), 1553–1568.

Bretherton, C. S., M. Widmann, V. P. Dymnikov, J. M. Wallace, and I. Bladé (1999), The effective number of spatial degrees of freedom of a time-varying field, *Journal of Climate*, *12*(7), 1990–2009.

Burgman, R. J., B. P. Kirtman, A. C. Clement, and H. Vazquez (2017), Model evidence for low-level cloud feedback driving persistent changes in atmospheric circulation and regional hydroclimate, *Geophysical Research Letters*, *44*(1), 428–437.

Carvalho, L. M., C. Jones, and B. Liebmann (2004), The South Atlantic Convergence Zone: Intensity, form, persistence, and relationships with intraseasonal to interannual activity and extreme rainfall, *Journal of Climate*, *17*(1), 88–108.

Chambers, D., B. Tapley, and R. Stewart (1999), Anomalous warming in the Indian Ocean coincident with El Niño, *Journal of Geophysical Research: Oceans*, *104*(C2), 3035–3047.

Chaves, R. R., and P. Nobre (2004), Interactions between sea surface temperature over the South Atlantic Ocean and the South Atlantic Convergence Zone, *Geophysical Research Letters*, *31*(3).

Chelton, D. B., M. G. Schlax, and R. M. Samelson (2011), Global observations of nonlinear mesoscale eddies, *Progress in Oceanography*, *91*(2), 167–216.

Chowdary, J., S.-P. Xie, H. Tokinaga, Y. M. Okumura, H. Kubota, N. Johnson, and X.-T. Zheng (2012), Interdecadal variations in ENSO teleconnection to the Indo–western Pacific for 1870–2007, *Journal of Climate*, *25*(5), 1722–1744.

Cravatte, S., T. Delcroix, D. Zhang, M. McPhaden, and J. Leloup (2009), Observed freshening and warming of the western Pacific warm pool, *Climate Dynamics*, *33*(4), 565–589.

De Almeida, R. A. F., P. Nobre, R. Haarsma, and E. Campos (2007), Negative Ocean-atmosphere feedback in the South Atlantic Convergence Zone, *Geophysical Research Letters*, *34*(18).

Delworth, T. L., F. Zeng, A. Rosati, G. A. Vecchi, and A. T. Wittenberg (2015), A link between the hiatus in global warming and North American drought, *Journal of Climate*, *28*(9), 3834–3845.

Deser, C., M. A. Alexander, S.-P. Xie, and A. S. Phillips (2010), Sea surface temperature variability: Patterns and mechanisms, *Annual review of marine science*, *2*, 115–143.

Dommenget, D., and M. Latif (2002), A cautionary note on the interpretation of EOFs, *Journal of climate*, *15*(2), 216–225.

Doyle, M. E., and V. R. Barros (2002), Midsummer low-level circulation and precipitation in subtropical South America and related sea surface temperature anomalies in the South Atlantic, *Journal of Climate*, *15*(23), 3394–3410.

Enfield, D. B., and D. A. Mayer (1997), Tropical Atlantic sea surface temperature variability and its relation to El Niño-Southern Oscillation, *Journal of Geophysical Research:*

Oceans, *102*(C1), 929–945.

Enfield, D. B., and A. M. Mestas-Nuñez (1999), Multiscale variabilities in global sea surface temperatures and their relationships with tropospheric climate patterns, *Journal of Climate*, *12*(9), 2719–2733.

Fedorov, A. V., S. Hu, M. Lengaigne, and E. Guilyardi (2015), The impact of westerly wind bursts and Ocean initial state on the development, and diversity of El Niño events, *Climate Dynamics*, *44*(5-6), 1381–1401.

Garzoli, S. L., and R. Matano (2011), The South Atlantic and the Atlantic meridional overturning circulation, *Deep Sea Research Part II: Topical Studies in Oceanography*, *58*(17), 1837–1847.

Goes, M., M. Cirano, M. Mata, and S. Majumder (2019), Long-term monitoring of the Brazil Current at 22S from XBT and altimetry data: seasonal, interannual and extreme variability, *JGR-Oceans*, *XX*(XX), XXX.

Grimm, A. M. (2003), The El Niño impact on the summer monsoon in Brazil: regional processes versus remote influences, *Journal of Climate*, *16*(2), 263–280.

Grimm, A. M. (2004), How do La Niña events disturb the summer monsoon system in Brazil?, *Climate Dynamics*, *22*(2-3), 123–138.

Grodsky, S. A., and J. A. Carton (2006), Interannual variation of sea level in the South Atlantic based on satellite altimetry., in *Earth ESA International Workshop. Venice.*

Haarsma, R. J., E. J. Campos, W. Hazeleger, C. Severijns, A. R. Piola, and F. Molteni (2005), Dominant modes of variability in the South Atlantic: A study with a hierarchy of Ocean–atmosphere models, *Journal of climate*, *18*(11), 1719–1735.

Hazeleger, W., F. Molteni, C. Severijns, R. Haarsma, A. Bracco, and F. Kucharski (2003), SPEEDO: a flexible coupled model for climate studies, *Clivar Exchanges*, *28*, 27–30.

Holbrook, N. J., I. D. Goodwin, S. McGregor, E. Molina, and S. B. Power (2011), Enso to multi-decadal time scale changes in East Australian Current transports and fort denison sea level: Oceanic Rossby waves as the connecting mechanism, *Deep Sea Research Part II: Topical Studies in Oceanography*, *58*(5), 547–558.

Jiang, N., J. D. Neelin, and M. Ghil (1995), Quasi-quadrennial and quasi-biennial variability in the equatorial pacific, *Climate Dynamics*, *12*(2), 101–112.

Kalnay, E., M. Kanamitsu, R. Kistler, W. Collins, D. Deaven, L. Gandin, M. Iredell, S. Saha, G. White, J. Woollen, et al. (1996), The NCEP/NCAR 40-year reanalysis project, *Bulletin of the American meteorological Society*, *77*(3), 437–472.

Kao, H.-Y., and J.-Y. Yu (2009), Contrasting eastern-Pacific and central-Pacific types of ENSO, *Journal of Climate*, *22*(3), 615–632.

Kwon, Y.-O., and C. Deser (2007), North Pacific decadal variability in the community climate system model version 2, *Journal of climate*, *20*(11), 2416–2433.

Lean, J. L., and D. H. Rind (2008), How natural and anthropogenic influences alter global and regional surface temperatures: 1889 to 2006, *Geophysical Research Letters*, *35*(18).

Lee, S.-K., H. Lopez, E.-S. Chung, P. DiNezio, S.-W. Yeh, and A. T. Wittenberg (2018), On the fragile relationship between El Niño and California rainfall, *Geophysical Research Letters*, *45*(2), 907–915.

Lee, T., and M. J. McPhaden (2010), Increasing intensity of el niño in the central-equatorial pacific, *Geophysical Research Letters*, *37*(14).

Li, J., S.-P. Xie, E. R. Cook, G. Huang, R. D'arrigo, F. Liu, J. Ma, and X.-T. Zheng (2011), Interdecadal modulation of El Niño amplitude during the past millennium, *Nature climate change*, *1* (2), 114.

Liu, Y., X. San Liang, and R. H. Weisberg (2007), Rectification of the bias in the wavelet power spectrum, *Journal of Atmospheric and Oceanic Technology*, *24* (12), 2093–2102.

Liu, Y., K. M. Cobb, H. Song, Q. Li, C.-Y. Li, T. Nakatsuka, Z. An, W. Zhou, Q. Cai, J. Li, et al. (2017), Recent enhancement of central Pacific El Niño variability relative to last eight centuries, *Nature communications*, *8*, 15,386.

Lopez, H., S. Dong, S.-K. Lee, and G. Goni (2016a), Decadal modulations of interhemispheric global atmospheric circulations and monsoons by the South Atlantic meridional overturning circulation, *Journal of Climate*, *29* (5), 1831–1851.

Lopez, H., S. Dong, S.-K. Lee, and E. Campos (2016b), Remote influence of Interdecadal Pacific Oscillation on the South Atlantic meridional overturning circulation variability, *Geophysical Research Letters*, *43* (15), 8250–8258.

Maharaj, A. M., P. Cipollini, and N. J. Holbrook (2005), Observed variability of the South Pacific westward sea level anomaly signal in the presence of bottom topography, *Geophysical research letters*, *32* (4).

Maharaj, A. M., N. J. Holbrook, and P. Cipollini (2009), Multiple westward propagating signals in South Pacific sea level anomalies, *Journal of Geophysical Research: Oceans*, *114* (C12).

Majumder, S., and C. Schmid (2018), A study of the variability in the Benguela Current volume transport, *Ocean Science*, *14* (2), 273–283.

McPhaden, M., T. Lee, and D. McClurg (2011), El Niño and its relationship to changing background conditions in the tropical Pacific Ocean, *Geophysical Research Letters*, *38*(15).

Merrifield, M., and R. Guza (1990), Detecting propagating signals with complex empirical orthogonal functions: A cautionary note, *Journal of physical oceanography*, *20*(10), 1628–1633.

Mo, K. C., and R. W. Higgins (1998), The Pacific–South American modes and tropical convection during the Southern Hemisphere winter, *Monthly Weather Review*, *126*(6), 1581–1596.

Mo, K. C., and J. N. Paegle (2001), The Pacific–South American modes and their downstream effects, *International Journal of Climatology: A Journal of the Royal Meteorological Society*, *21*(10), 1211–1229.

Morioka, Y., T. Tozuka, and T. Yamagata (2011), On the growth and decay of the subtropical dipole mode in the South Atlantic, *Journal of Climate*, *24*(21), 5538–5554.

Navarra, A., and V. Simoncini (2010), Generalizations: Rotated, complex, extended and combined eof, in *A Guide to Empirical Orthogonal Functions for Climate Data Analysis*, pp. 69–96, Springer.

Nobre, P., R. A. De Almeida, M. Malagutti, and E. Giarolla (2012), Coupled Ocean–atmosphere variations over the South Atlantic Ocean, *Journal of Climate*, *25*(18), 6349–6358.

Ogata, T., S.-P. Xie, A. Wittenberg, and D.-Z. Sun (2013), Interdecadal amplitude modulation of El Niño–Southern Oscillation and its impact on tropical Pacific decadal variability, *Journal of Climate*, *26*(18), 7280–7297.

O'Kane, T., R. Matear, M. Chamberlain, E. Oliver, and N. Holbrook (2014), Storm tracks in the Southern Hemisphere subtropical oceans, *Journal of Geophysical Research: Oceans*, *119*(9), 6078–6100.

Osychny, V. (2006), Analysis of the Gulf Stream path and Rossby waves in the North Atlantic based on satellite data, PhD dissertation, University of Rhode Island.

Palastanga, V., C. S. Vera, and A. R. Piola (2002), On the leading modes of sea surface temperature variability in the South Atlantic Ocean, *Clivar Exchanges*, *7*(3-4), 12–15.

Polito, P. S., and W. T. Liu (2003), Global characterization of Rossby waves at several spectral bands, *Journal of Geophysical Research: Oceans*, *108*(C1).

Polito, P. S., and O. T. Sato (2015), Do eddies ride on Rossby waves?, *Journal of Geophysical Research: Oceans*, *120*(8), 5417–5435.

Reynolds, R. W., T. M. Smith, C. Liu, D. B. Chelton, K. S. Casey, and M. G. Schlax (2007), Daily high-resolution-blended analyses for sea surface temperature, *Journal of Climate*, *20*(22), 5473–5496.

Rodrigues, R. R., E. J. Campos, and R. Haarsma (2015), The impact of ENSO on the South Atlantic subtropical dipole mode, *Journal of Climate*, *28*(7), 2691–2705.

Sasaki, Y. N., S. Minobe, and N. Schneider (2013), Decadal response of the Kuroshio Extension jet to Rossby waves: Observation and thin-jet theory, *Journal of Physical Oceanography*, *43*(2), 442–456.

Schmid, C., and S. Majumder (2018), Transport variability of the Brazil Current from observations and a data assimilation model, *Ocean Science*, *14*(3), 417–436.

Sterl, A., and W. Hazeleger (2003), Coupled variability and air-sea interaction in the South Atlantic Ocean, *Climate Dynamics*, *21*(7-8), 559–571.

Suzuki, R., S. K. Behera, S. Iizuka, and T. Yamagata (2004), Indian Ocean subtropical dipole simulated using a coupled general circulation model, *Journal of Geophysical Research: Oceans*, *109*(C9).

Taschetto, A. S., A. S. Gupta, N. C. Jourdain, A. Santoso, C. C. Ummenhofer, and M. H. England (2014), Cold Tongue and Warm Pool ENSO Events in CMIP5: Mean State and Future Projections, *Journal of Climate*, *27*(8), 2861–2885, doi:10.1175/JCLI-D-13-00437.1.

Timmermann, A., S.-I. An, J.-S. Kug, F.-F. Jin, W. Cai, A. Capotondi, K. Cobb, M. Lengaigne, M. J. McPhaden, M. F. Stuecker, et al. (2018), El nino–Southern oscillation complexity, *Nature*, *559*(7715), 535.

Torrence, C., and G. P. Compo (1998), A practical guide to wavelet analysis, *Bulletin of the American Meteorological society*, *79*(1), 61–78.

Trenberth, K. E., and D. P. Stepaniak (2001), Indices of El Niño evolution, *Journal of Climate*, *14*(8), 1697–1701.

Venegas, S., L. Mysak, and D. Straub (1997), Atmosphere–Ocean coupled variability in the South Atlantic, *Journal of Climate*, *10*(11), 2904–2920.

Wang, B., and Y. Wang (1996), Temporal structure of the southern oscillation as revealed by waveform and wavelet analysis, *Journal of Climate*, *9*(7), 1586–1598.

Wittenberg, A. T., A. Rosati, T. L. Delworth, G. A. Vecchi, and F. Zeng (2014), ENSO modulation: Is it decadally predictable?, *Journal of Climate*, *27*(7), 2667–2681.

Xie, S.-P., C. Deser, G. A. Vecchi, J. Ma, H. Teng, and A. T. Wittenberg (2010), Global warming pattern formation: Sea surface temperature and rainfall, *Journal of Climate*, *23*(4), 966–986.

Xie, S.-P., C. Deser, G. A. Vecchi, M. Collins, T. L. Delworth, A. Hall, E. Hawkins, N. C. Johnson, C. Cassou, A. Giannini, et al. (2015), Towards predictive understanding of regional climate change, *Nature Climate Change*, *5*(10), 921.

Yu, J.-Y., and S. T. Kim (2010), Identification of central-Pacific and eastern-Pacific types of ENSO in CMIP3 models, *Geophysical Research Letters*, *37*(15).

Yu, J.-Y., P.-k. Kao, H. Paek, H.-H. Hsu, C.-w. Hung, M.-M. Lu, and S.-I. An (2015), Linking emergence of the central Pacific El Niño to the Atlantic multidecadal oscillation, *Journal of Climate*, *28*(2), 651–662.

Yu, J.-Y., X. Wang, S. Yang, H. Paek, and M. Chen (2017), The changing El Niño–Southern oscillation and associated climate extremes, *Climate Extremes: Patterns and Mechanisms*, pp. 1–38.

Table 1. Correlation coefficients and the respective p-values (in parenthesis) of the PCs and different El Niño indices. P-values are calculated using the effective number of degrees of freedom (df) given the autocorrelation of the time series. **Effective number of degrees of freedom corresponding to the CEOFs are shown in parentheses in the top row.**

Indices	CEOF1 (**14**)	CEOF2 (**19**)	CEOF3 (**21**)
ATNI:	0.31 (0.225)	0.23 (0.364)	**0.66** (0.007)
EMI:	0.38 (0.118)	0.10 (0.675)	**0.69** (0.009)
PDO:	**0.63** (0.044)	0.29 (0.207)	0.31 (0.152)
NINO34:	0.53 (0.052)	0.27 (0.240)	0.29 (0.223)
NINO3:	0.53 (0.063)	0.29 (0.215)	0.16 (0.454)
NINO4:	0.52 (0.052)	0.26 (0.270)	0.46 (0.072)
PSA2:	0.37 (0.183)	0.41 (0.059)	0.19 (0.442)

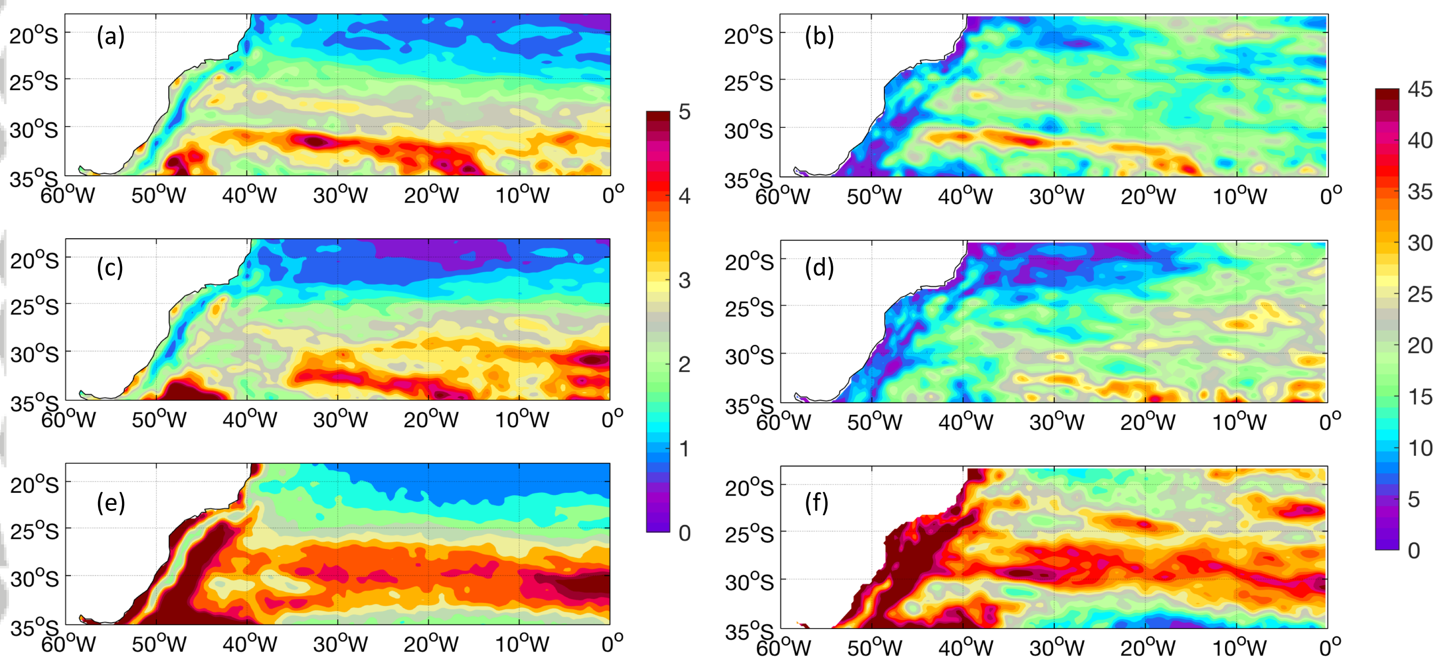

Figure 1. Standard deviation of SSH (cm) fields at interannual (a), semiannual (c, 168 and 456 days) and mesoscale (e, periods between 22 and 168 days) periods. SSH fields are bandpassed using a wavelet filter. Fraction (%) of variance explained by interannual (b), semiannual (d) and mesoscale (f) components of the SSH field. Fraction of variance was estimated by dividing the variance of interannual, semiannual and mesoscale SSH with the variance of detrended total SSH.

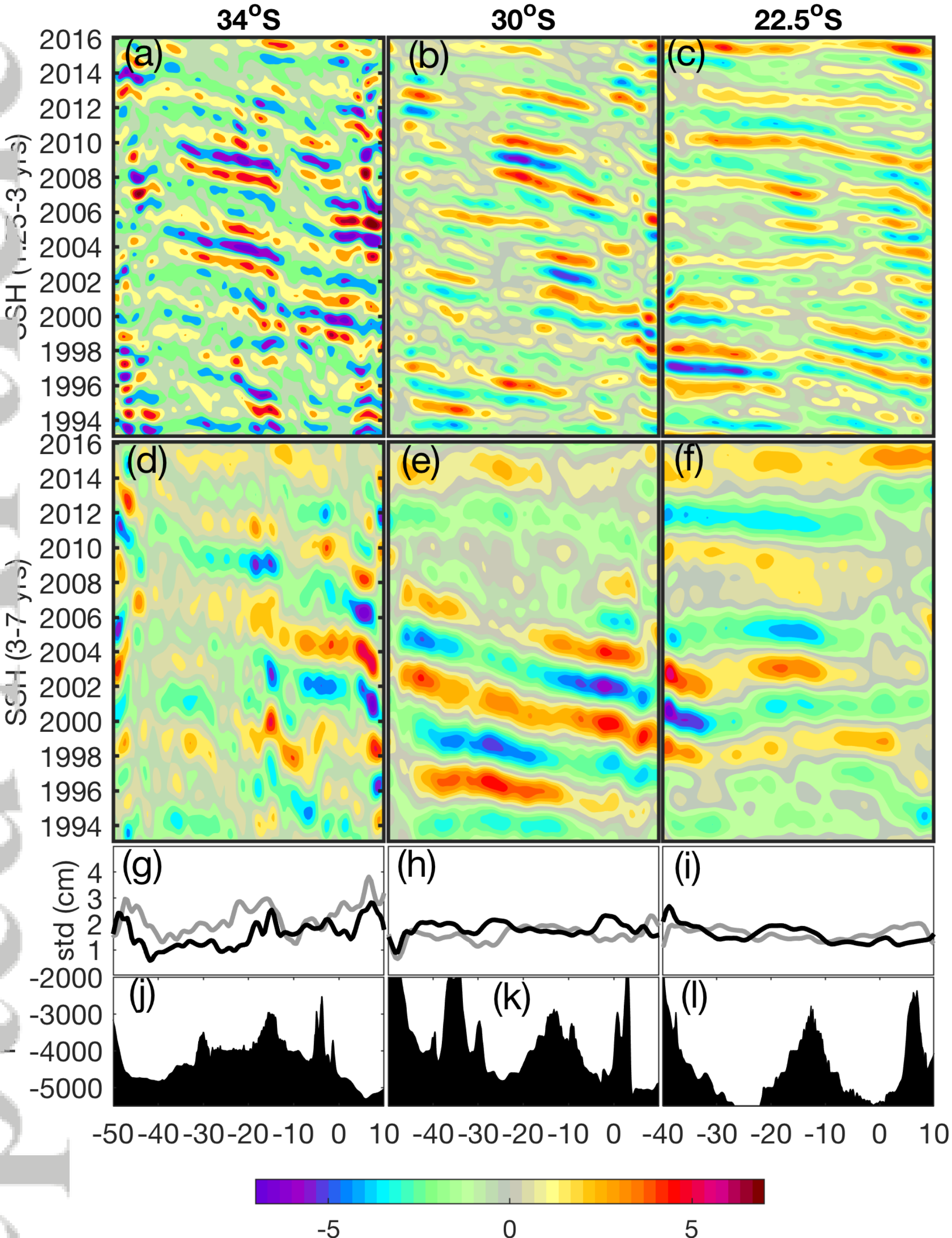

Figure 2. (a, b, c) Hovmöller diagrams of bandpassed SSH (in cm) between 1.25 and 3 years for 34°S, 30°S and 22.5°S. (d, e ,f) The same for bandpassed SSH between 3 and 7 years. (g, h, i) Standard deviations of bandpassed SSH for 1.25 -3 years (gray) and 3-7 years (black). Black and gray lines represent. (j, k, l) The local bathymetry at the corresponding latitudes. SSH at 22.5°S is multiplied by a factor 2 to use the same color bar.

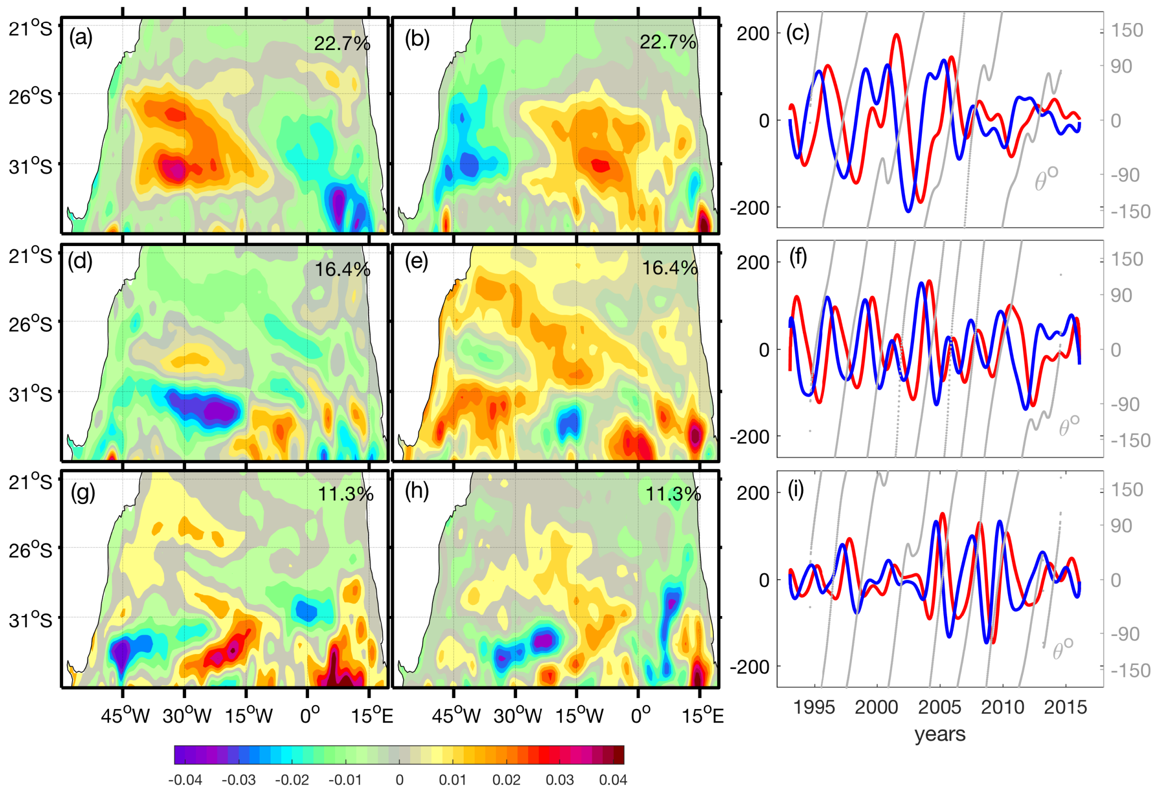

Figure 3. Interannual frequency (1.25-7 years) - Real (a, d, g) and imaginary (b, e, h) components of the first three CEOF modes. (c, f, i) Corresponding real (red) and imaginary (blue) expansion coefficients and temporal phases (gray). By definition, the real and imaginary maps and PCs have a 90 degree phase lag, showing propagation.

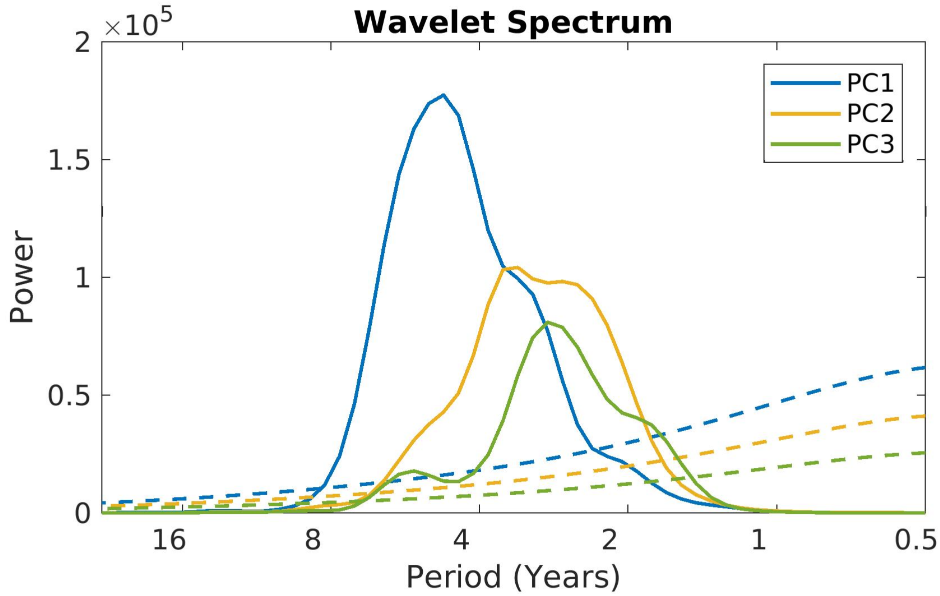

Figure 4. Wavelet spectra (solid colored lines) of the first 3 CEOF PCs. Dashed lines are their respective confidence limit.

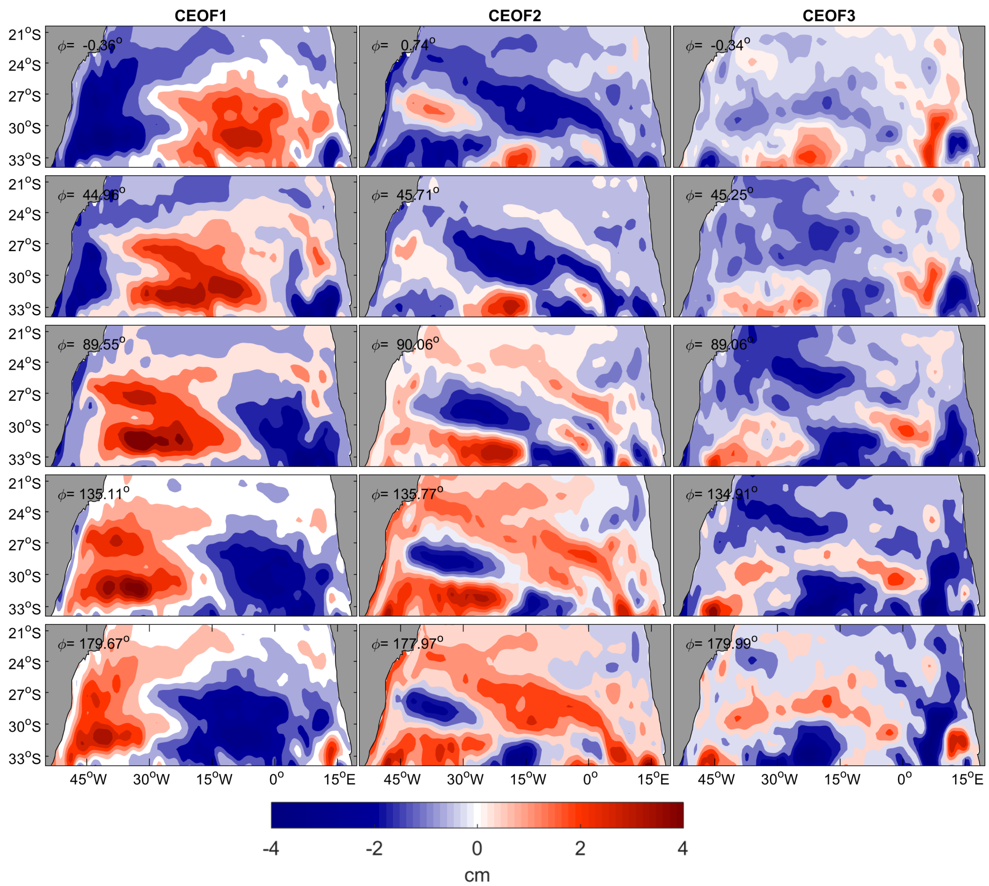

Figure 5. Re-construction of the first 3 CEOF modes (left to right) at interannual frequency (1.25-7 years) showing one full cycle (0-180 degrees) rotated every 45 degree phase intervals (top to bottom). Rotated angle is shown on the top left of each panel.

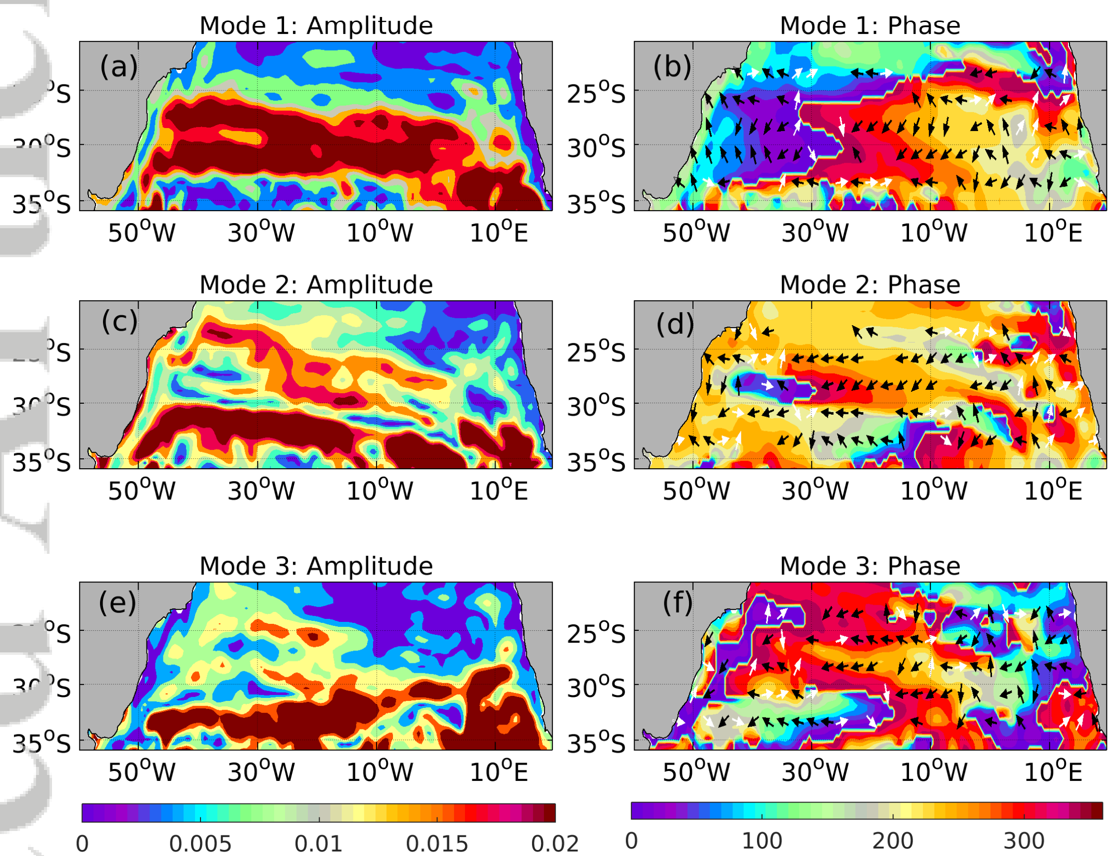

Figure 6. (a, c, e) Amplitudes and (b, d, f) spatial phases (Φ) of the first three CEOF modes. Arrows on the right panels are the normalized phase velocities for the corresponding modes. White and black arrows represent eastward and westward propagations respectively. Propagating patterns follow the gradients of the spatial phase, from negative to positive. Dominance of westward propagating features is clear in all modes.

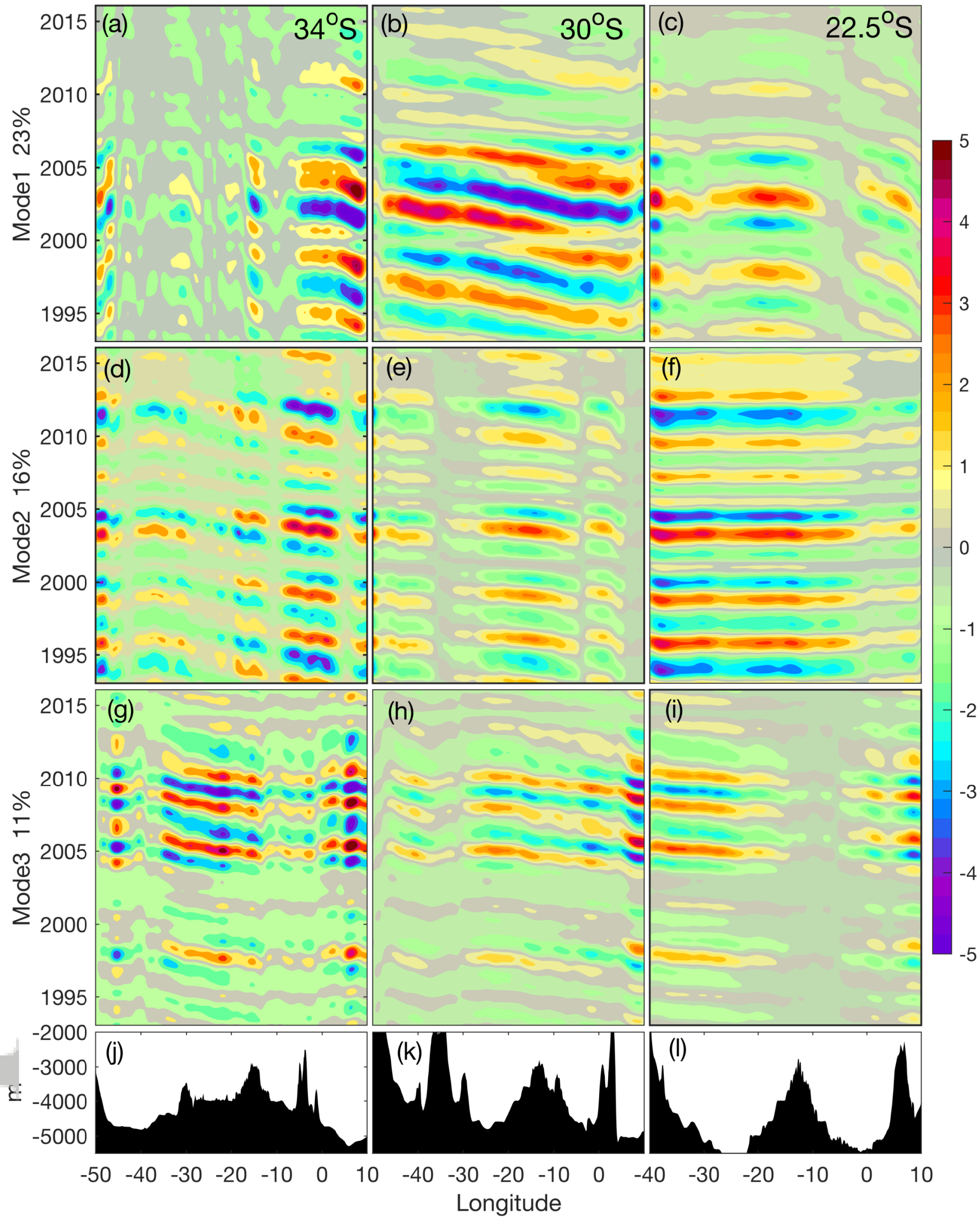

Figure 7. Hovmöller plots of the reconstructed SSH (cm) using CEOF1 (a, b, c), CEOF2 (d, e, f) and CEOF3 (g, h, i) along 34°S, 30°S, and 22.5°S. (j, k, l) Corresponding local bathymetry.

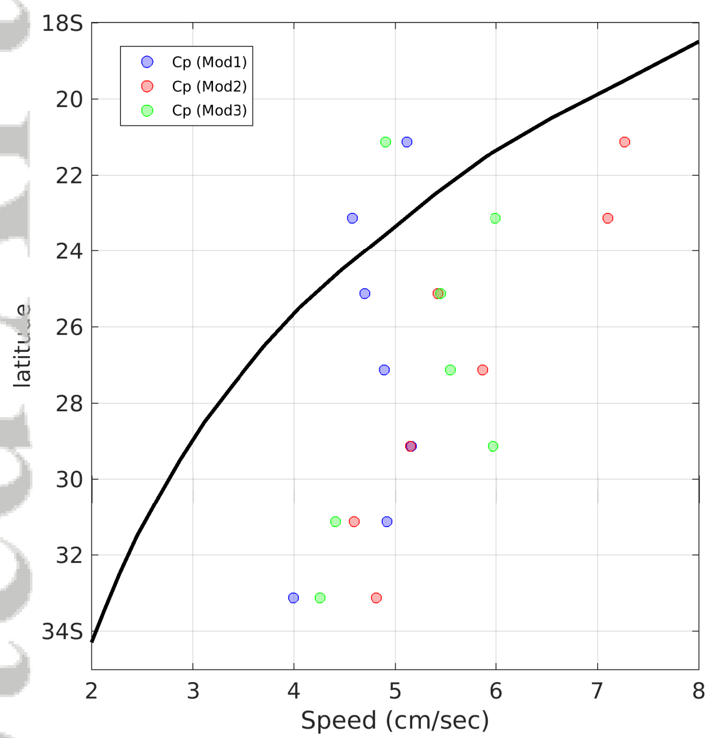

Figure 8. Latitudinal variation of phase velocities for different CEOF modes, and the theoretical Rossby wave speed for the first baroclinic mode (black curve).

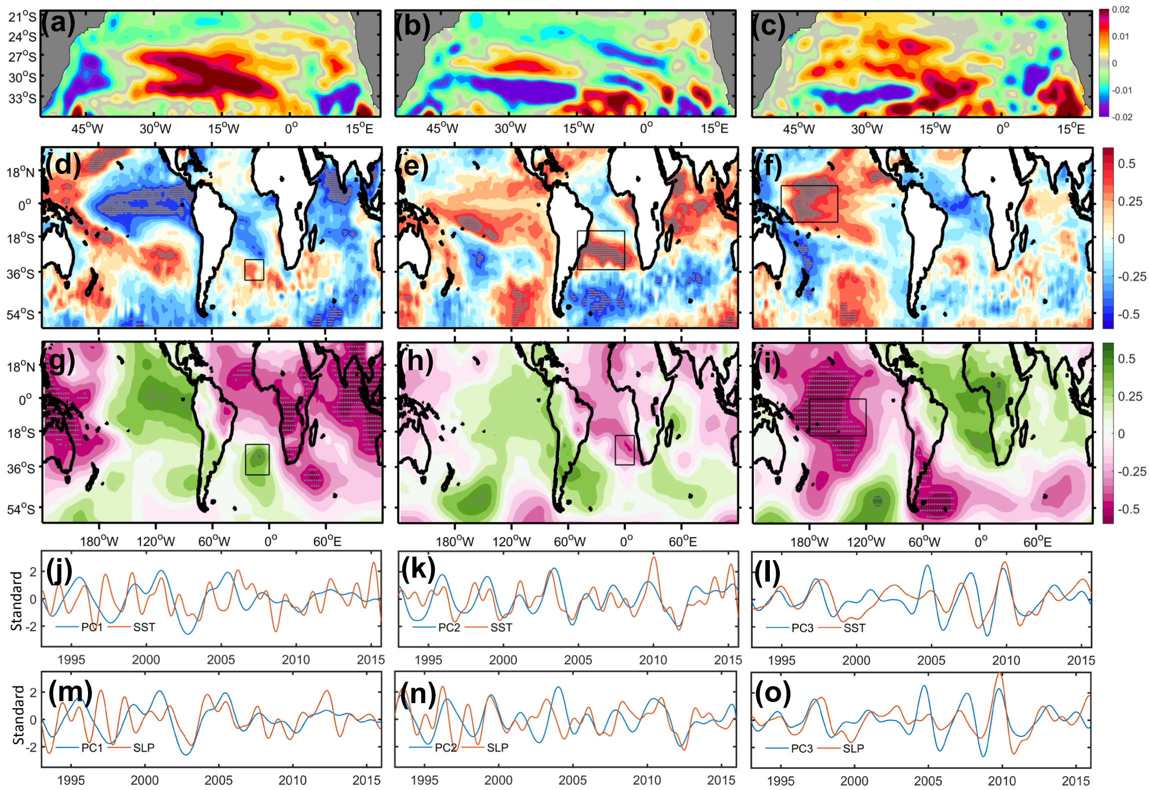

Figure 9. Left to right (a - c): Real part of the spatial patterns of the first three CEOF modes. (d - f) Point-wise instantaneous correlation between SST and the PCs of first three CEOFs at interannual timescales. **(g - i)** The same for SLP. Dotted regions of the maps represent 95% significant levels. (j - l) Time series of average reconstructed SST and PCs over the area (shown by rectangular boxes) with maximum correlation. (m - o) The same for SLP.

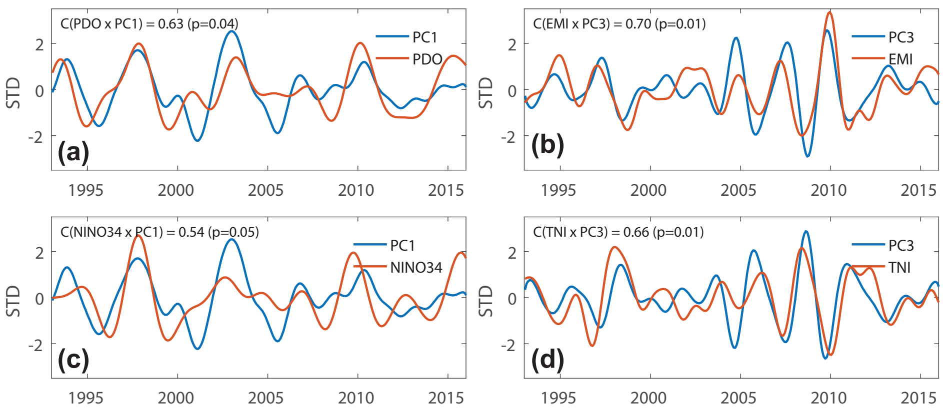

Figure 10. Time series of the PC1 and PC3 with the most correlated Niño indices from Table 1. (a, c) PC1 with PDO and Niño3.4 indices; (b, d) PC3 with EMI and TNI indices. PC time series are rotated to follow the same phase as the indices. Correlations (C) and P values (for the statistical significance) are indicated in text.

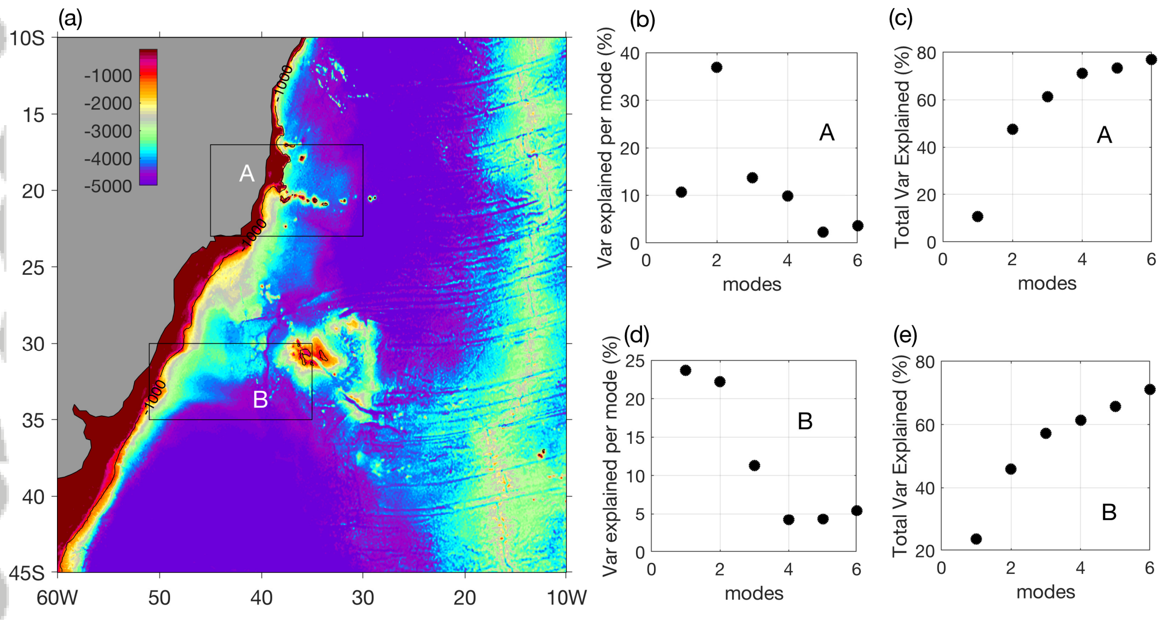

Figure 11. (a) Local topography near the Brazilian Coast. (b, d) Variance explained by individual modes and a combination of them (c, e) for areas A and B enclosing the **cross** section across which volume transport of the BC is estimated (at 22.5°S and at 34°S).

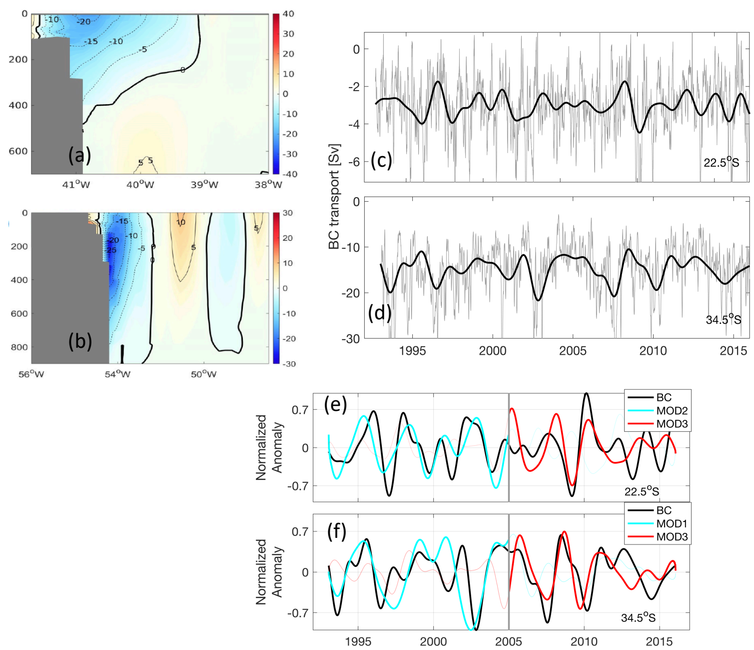

Figure 12. Cross section of **mean** meridional velocity of the BC (a, b) and its daily transport time series (gray) over plotted with bandpassed (1.25 - 7 years) transports across 22.5°S (c), and 34.5°S (d). (e, f) Bandpassed normalized BC transport with PCs. The vertical line at 2005 represents the time before which the BC exhibits strong correlation with mode 2 (e, for 22.5°S) and mode 1 (f, for 34.5°S) and after that it correlates significantly with mode 3.

Figure 1.

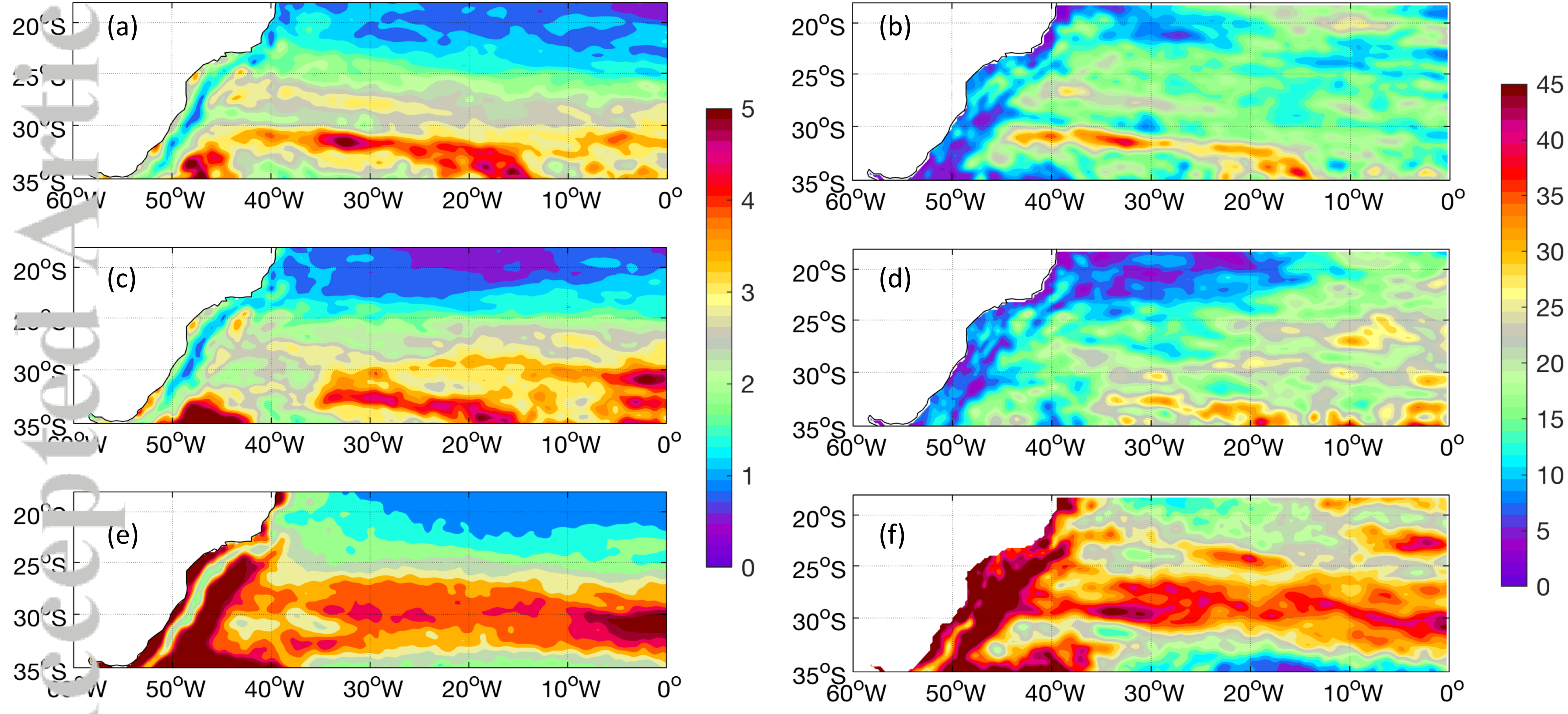
(a)
(b)
(c)
(d)
(e)
(f)
20°S
25°S
30°S
35°S
60°W
50°W
40°W
30°W
20°W
10°W
0°
0
1
2
3
4
5
0
5
10
15
20
25
30
35
40
45

Figure 2.

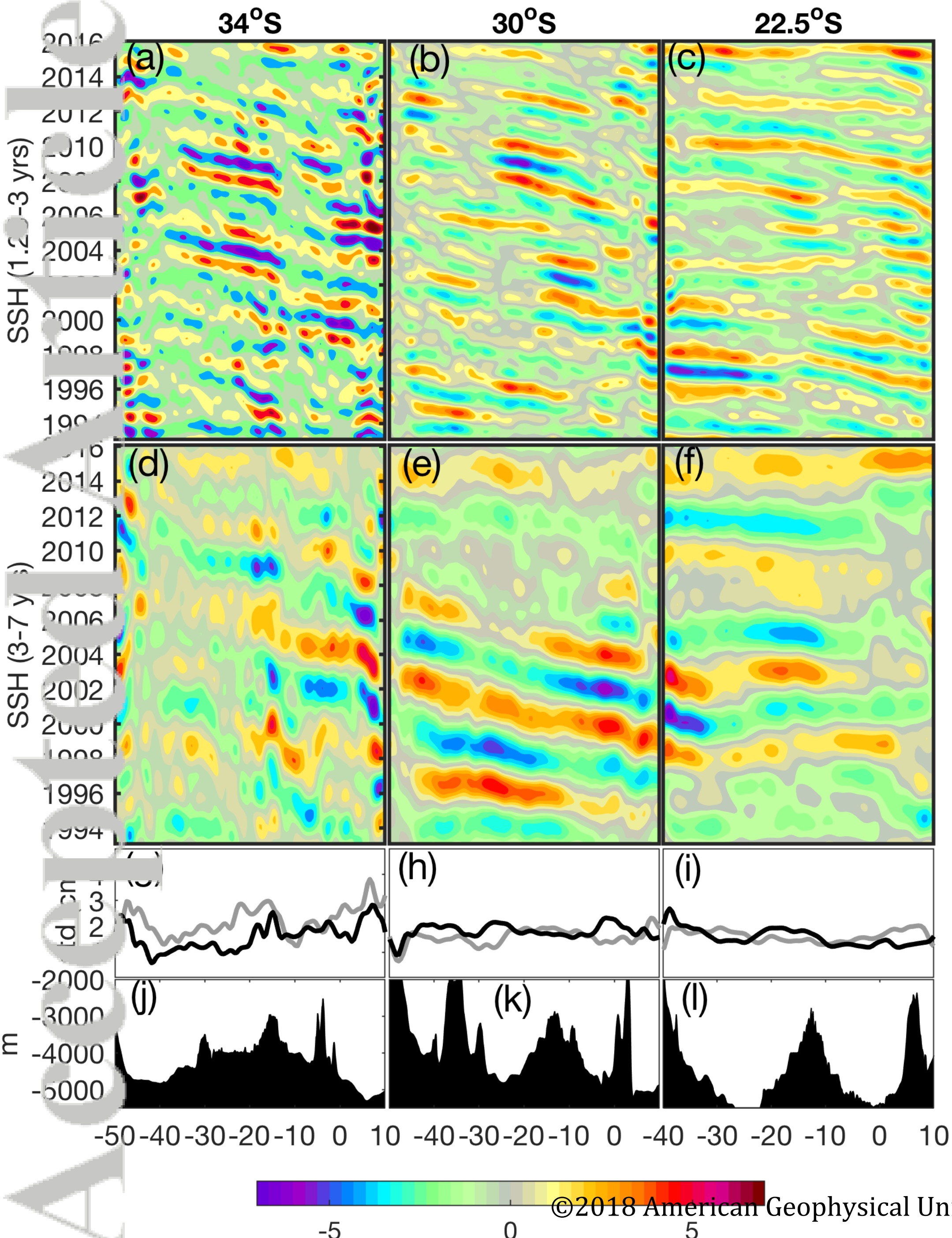

34°S
30°S
22.5°S
(a)
(b)
(c)
(d)
(e)
(f)
(h)
(i)
(j)
(k)
(l)
2014
2012
2010
2006
2004
2000
1996
2014
2012
2010
2004
2002
1996
SSH
SSH (3-7 y
3
2
-2000
-3000
-4000
-5000
m
-50 -40 -30 -20 -10 0 10 -40 -30 -20 -10 0 -40 -30 -20 -10 0 10
-5
0
5

Figure 3.

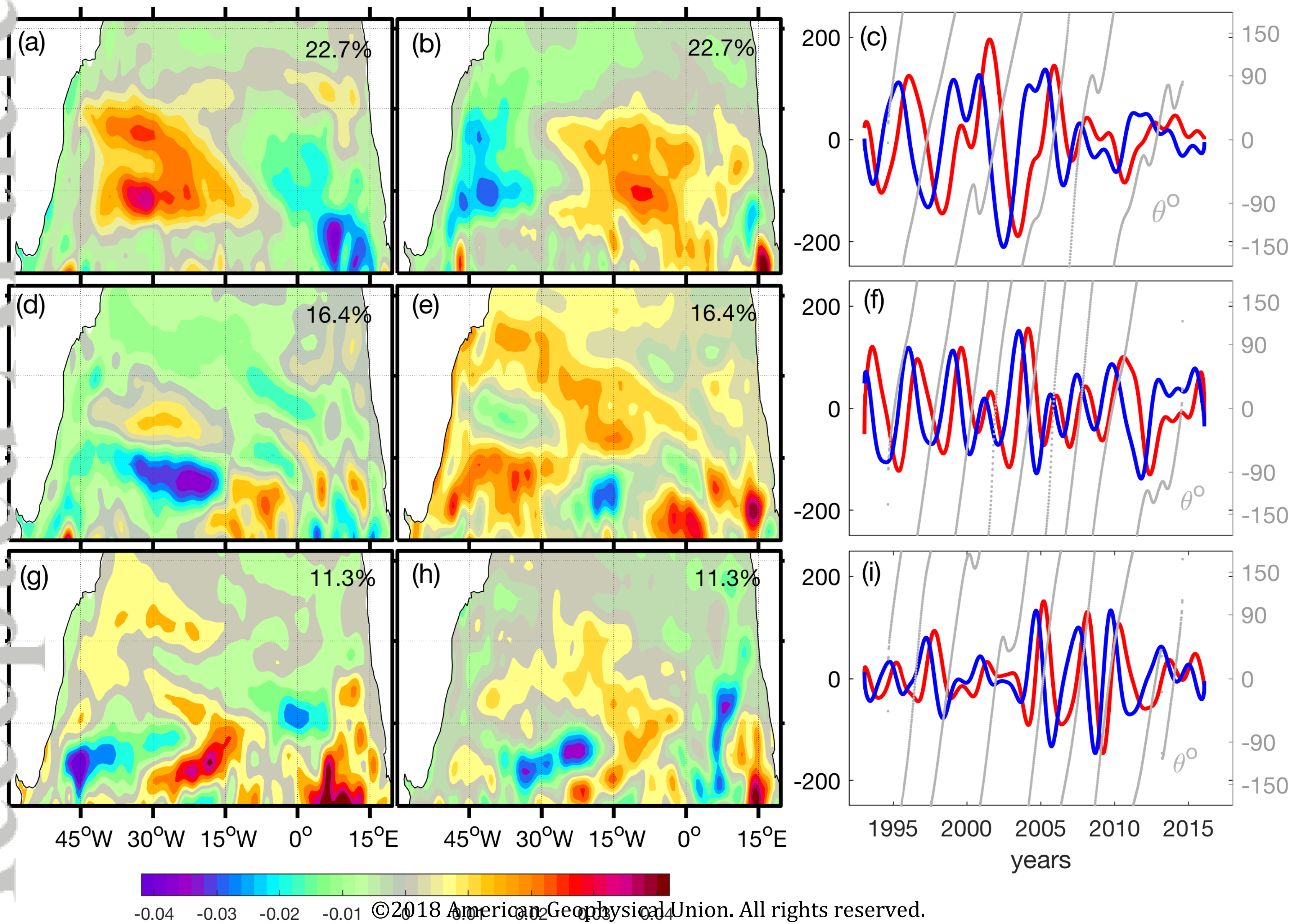
(a)
22.7%
(b)
22.7%
(c)
(d)
16.4%
(e)
16.4%
(f)
(g)
11.3%
(h)
11.3%
(i)
21°S
26°S
31°S
45°W 30°W 15°W 0° 15°E
200
0
-200
150
90
0
-90
-150
θ°
1995 2000 2005 2010 2015
years
-0.04 -0.03 -0.02 -0.01 0 0.01 0.02 0.03 0.04

Figure 4.

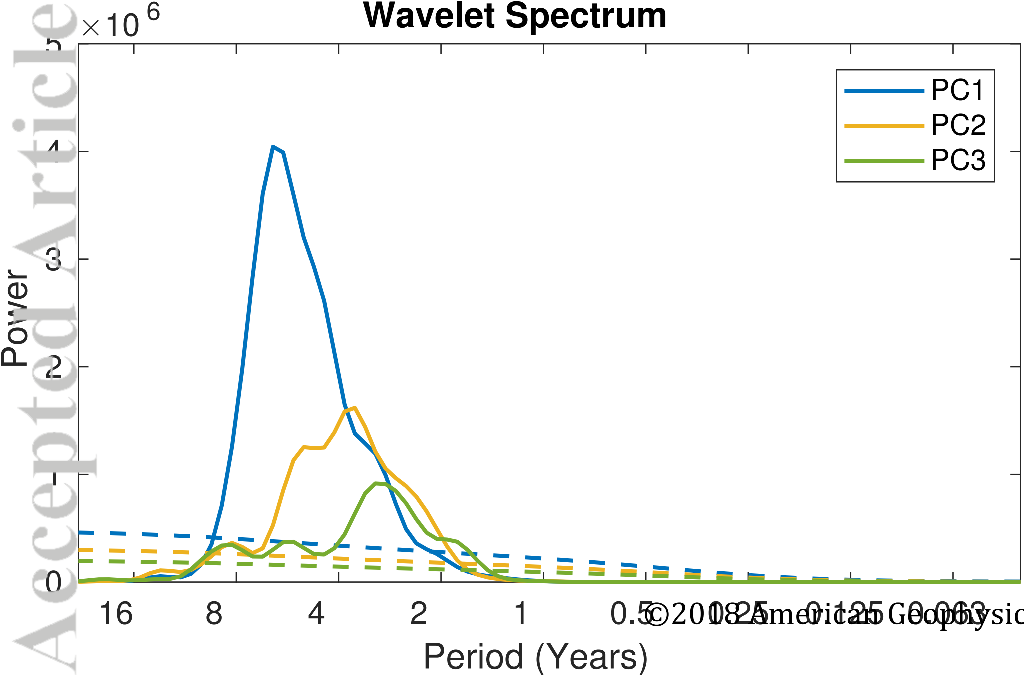
Wavelet Spectrum
×10^6
Power
Period (Years)
16
8
4
2
1
0.5
0.125
0.063
PC1
PC2
PC3

Figure 5.

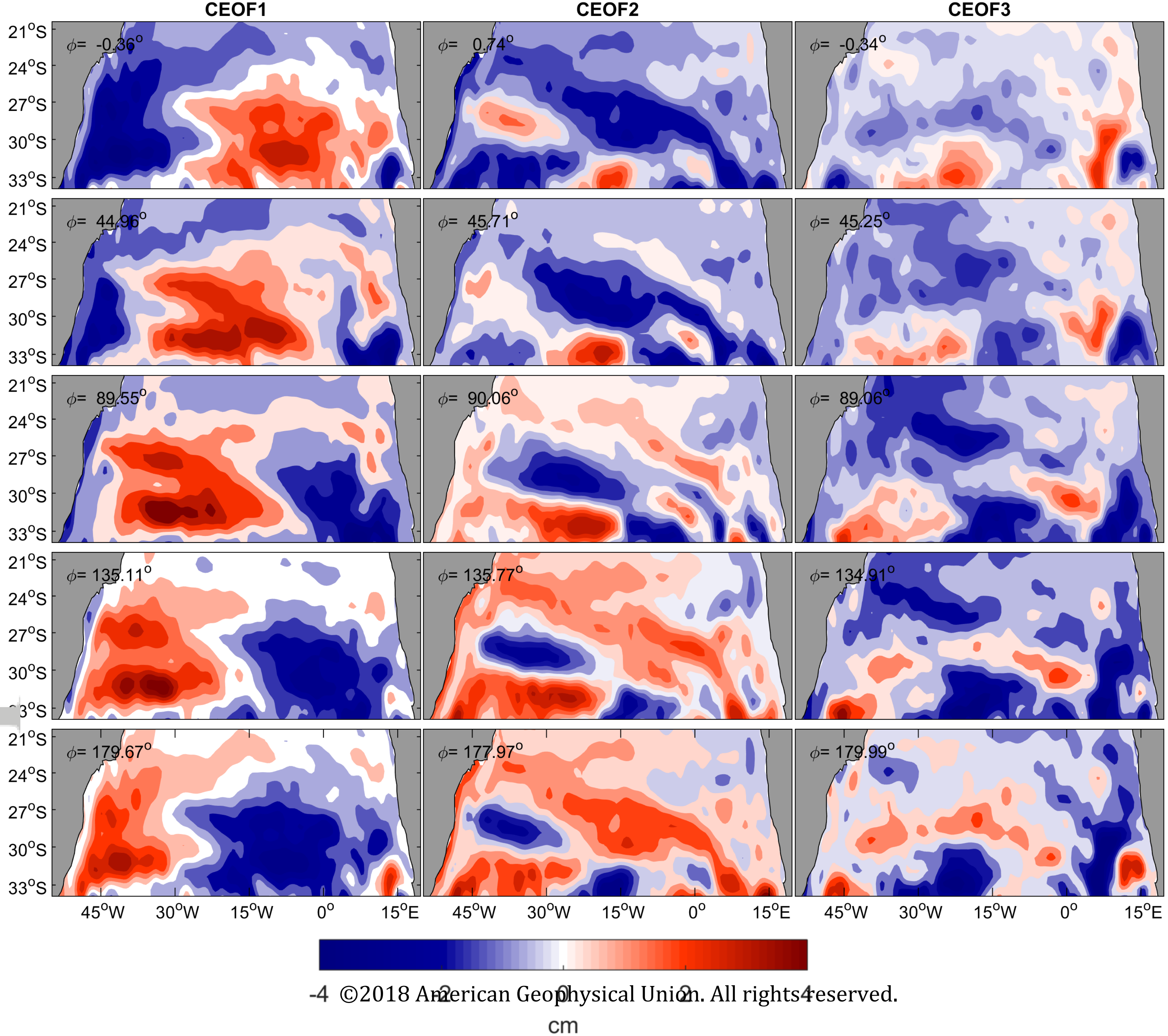
CEOF1
CEOF2
CEOF3
ϕ= -0.36°
ϕ= 0.74°
ϕ= -0.34°
ϕ= 44.96°
ϕ= 45.71°
ϕ= 45.25°
ϕ= 89.55°
ϕ= 90.06°
ϕ= 89.06°
ϕ= 135.11°
ϕ= 135.77°
ϕ= 134.91°
ϕ= 179.67°
ϕ= 177.97°
ϕ= 179.99°
21°S
24°S
27°S
30°S
33°S
45°W
30°W
15°W
0°
15°E
-4
-2
0
2
4
cm

Figure 6.

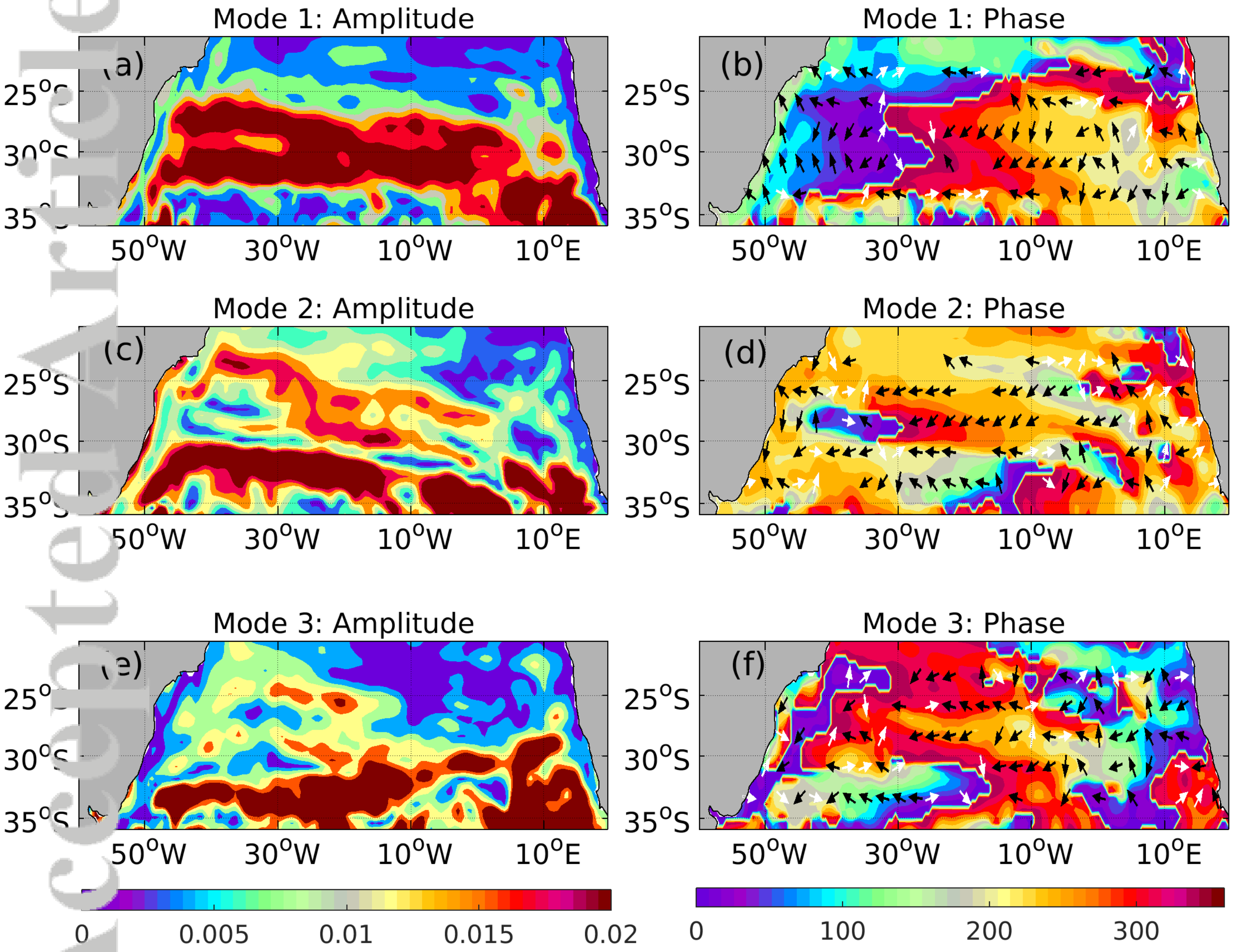
Mode 1: Amplitude
Mode 1: Phase
Mode 2: Amplitude
Mode 2: Phase
Mode 3: Amplitude
Mode 3: Phase
(a)
(b)
(c)
(d)
(e)
(f)
25^{o}S
30^{o}S
35^{o}S
50^{o}W
30^{o}W
10^{o}W
10^{o}E
0
0.005
0.01
0.015
0.02
0
100
200
300

Figure 7.

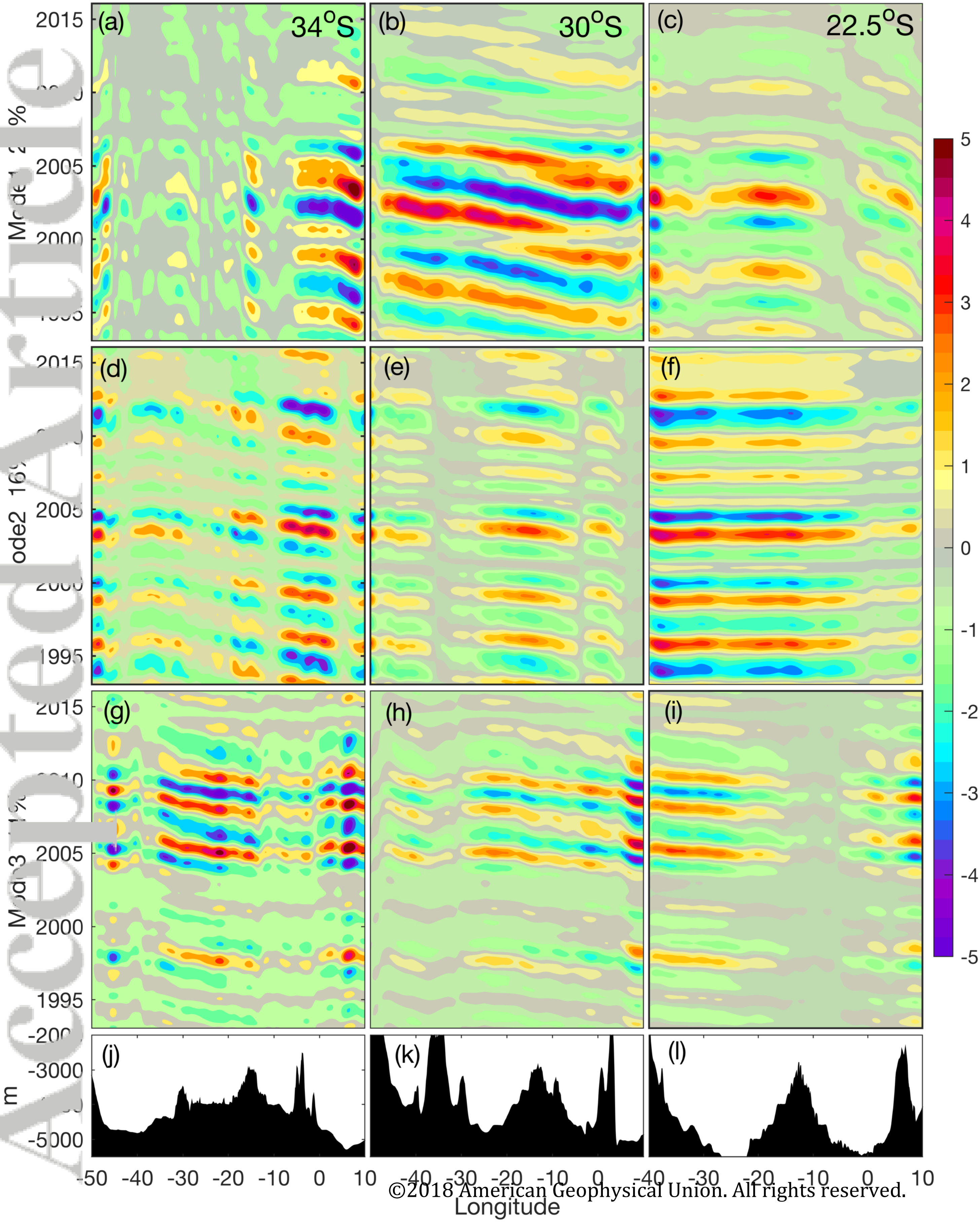

(a)
34°S
(b)
30°S
(c)
22.5°S
(d)
(e)
(f)
(g)
(h)
(i)
(j)
(k)
(l)
Longitude
m
-5000
-3000
2015
2005
2000
1995
5
4
3
2
1
0
-1
-2
-3
-4
-5
-50 -40 -30 -20 -10 0 10

Figure 8.

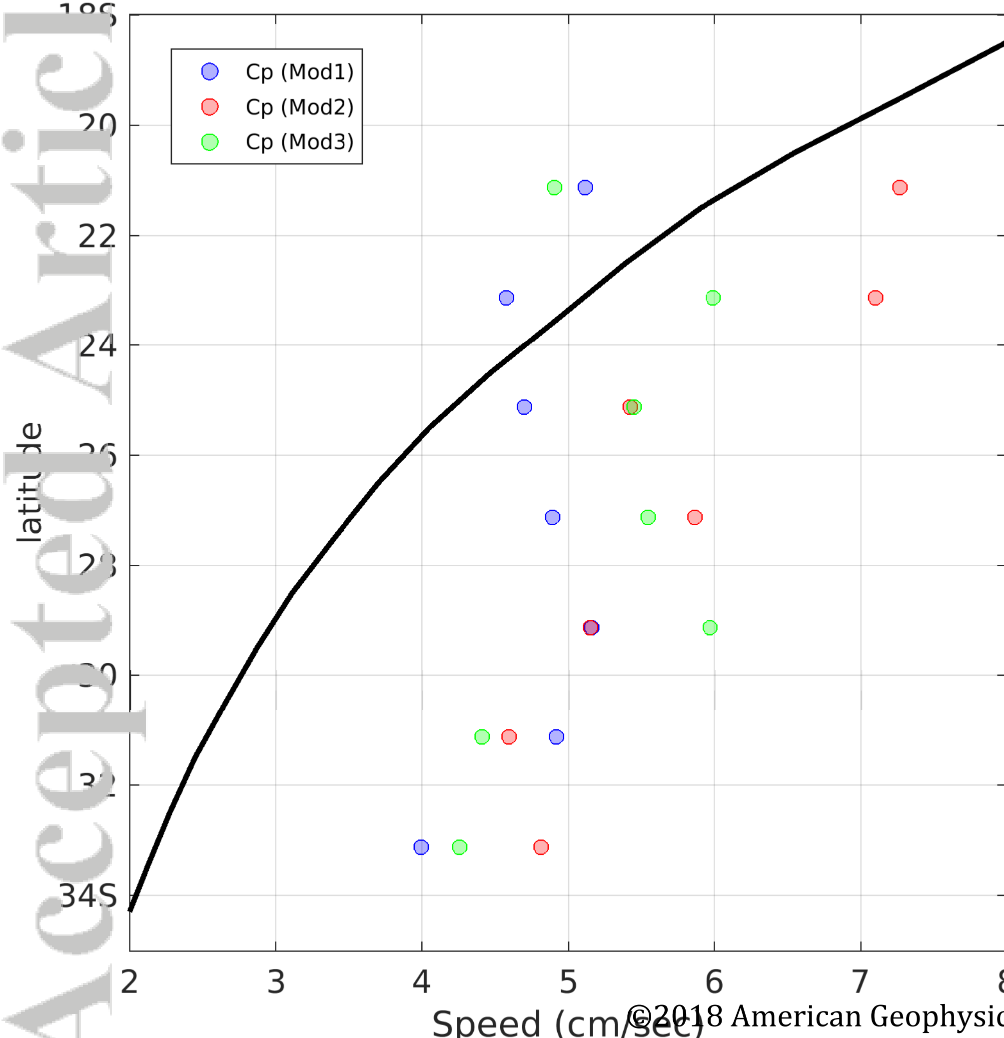
Cp (Mod1)
Cp (Mod2)
Cp (Mod3)
18S
20
22
24
26
28
30
32
34S
latitude
2
3
4
5
6
7
8
Speed (cm/sec)

Figure 9.

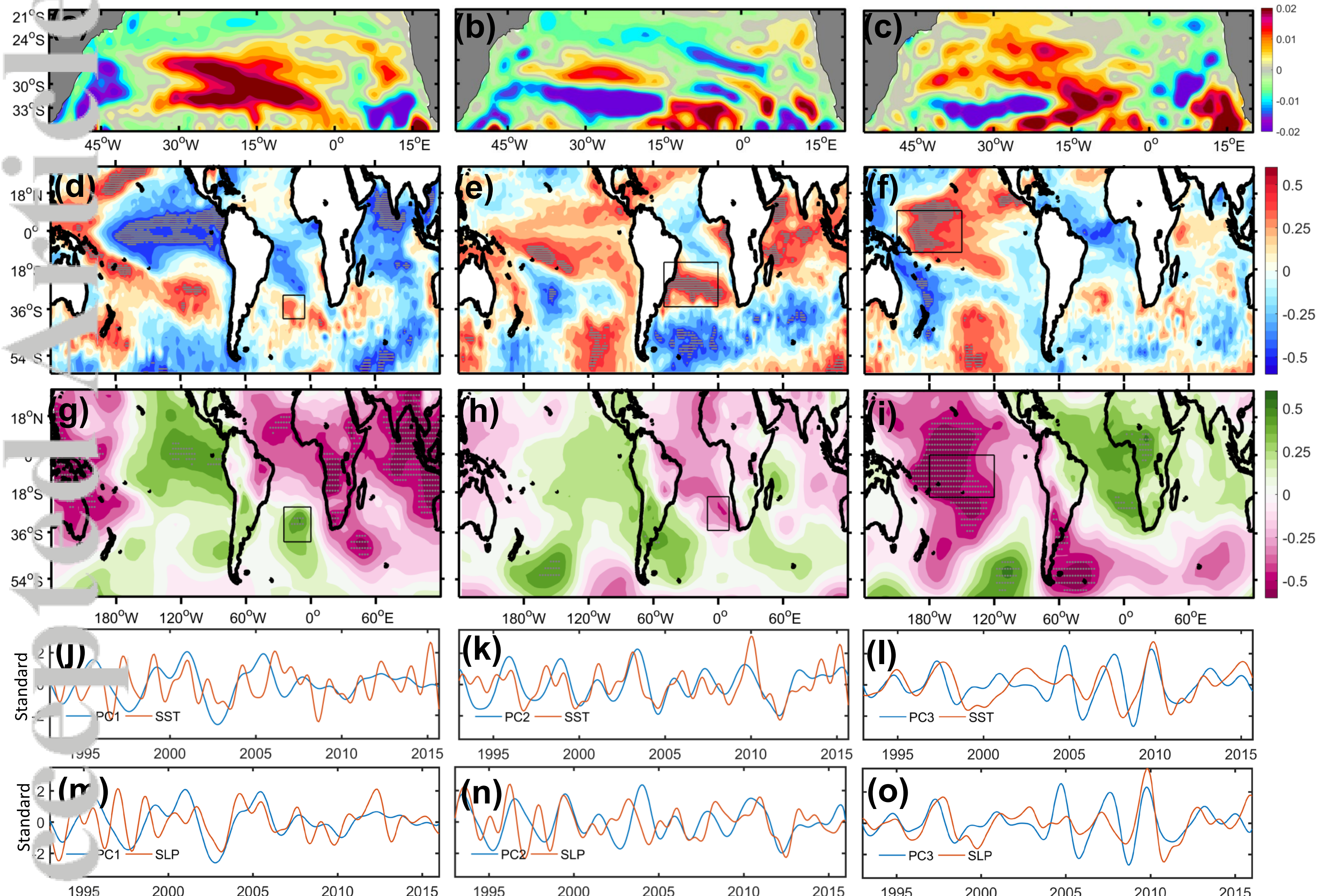
(b)
(c)
(d)
(e)
(f)
(g)
(h)
(i)
(j)
(k)
(l)
(n)
(o)
PC1
SST
PC2
PC3
SLP
Standard
1995
2000
2005
2010
2015

Figure 10.

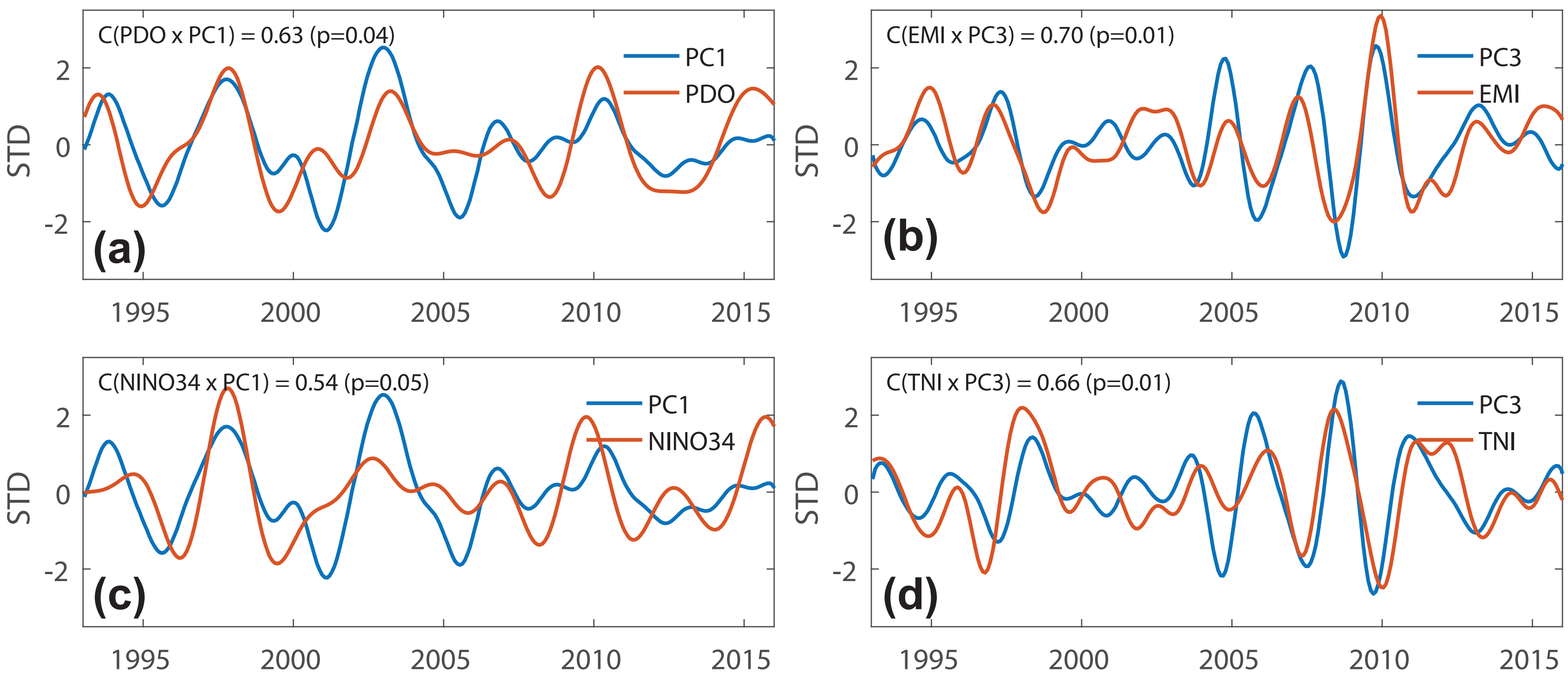

C(PDO x PC1) = 0.63 (p=0.04)
PC1
PDO
STD
(a)
C(EMI x PC3) = 0.70 (p=0.01)
PC3
EMI
(b)
C(NINO34 x PC1) = 0.54 (p=0.05)
PC1
NINO34
(c)
C(TNI x PC3) = 0.66 (p=0.01)
PC3
TNI
(d)
1995
2000
2005
2010
2015

Figure 11.

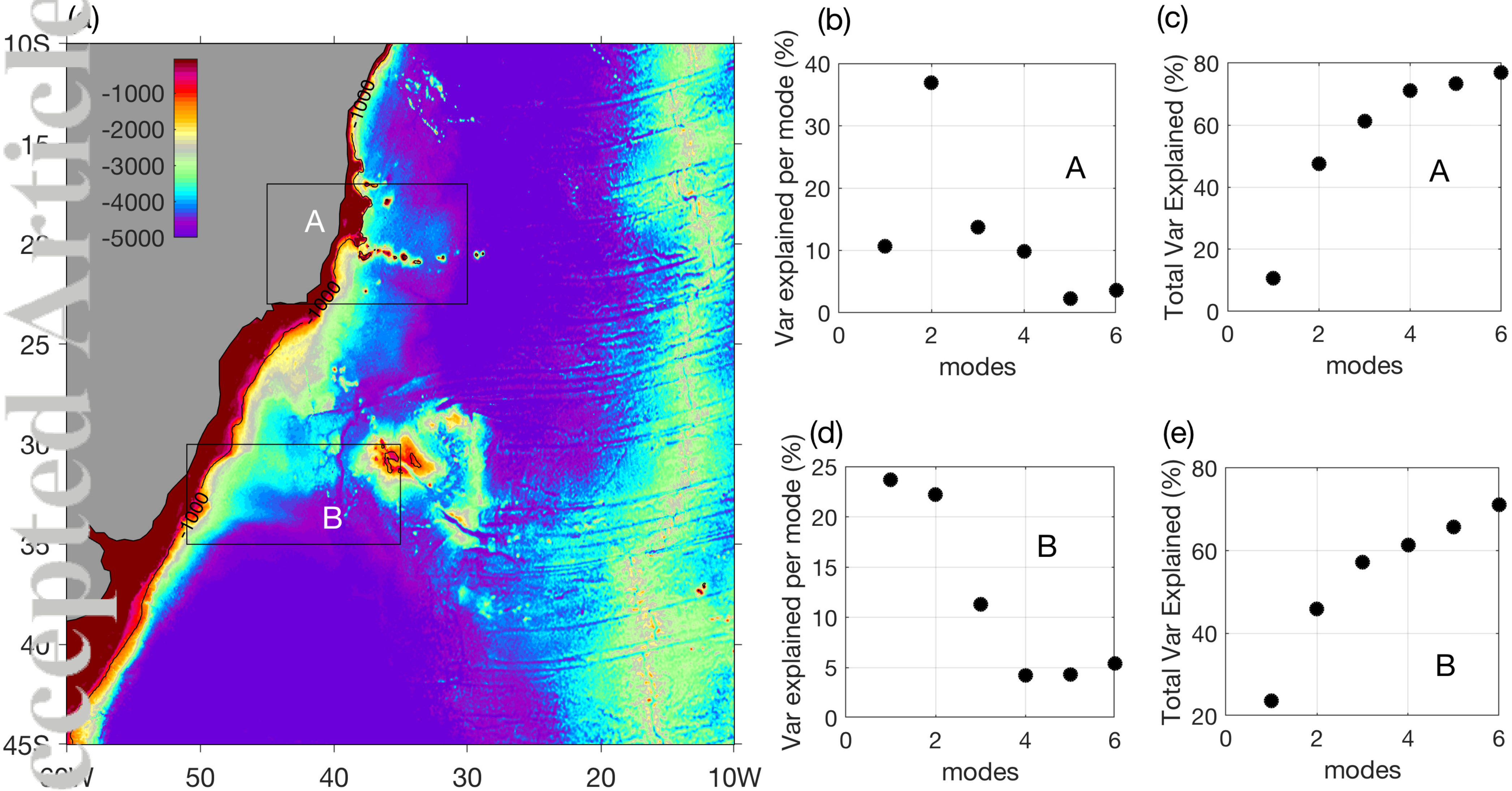
(a)
10S
15
20
25
30
35
40
45S
60W
50
40
30
20
10W
-1000
-2000
-3000
-4000
-5000
A
B
-1000
(b)
Var explained per mode (%)
modes
A
(c)
Total Var Explained (%)
modes
A
(d)
Var explained per mode (%)
modes
B
(e)
Total Var Explained (%)
modes
B

Figure 12.

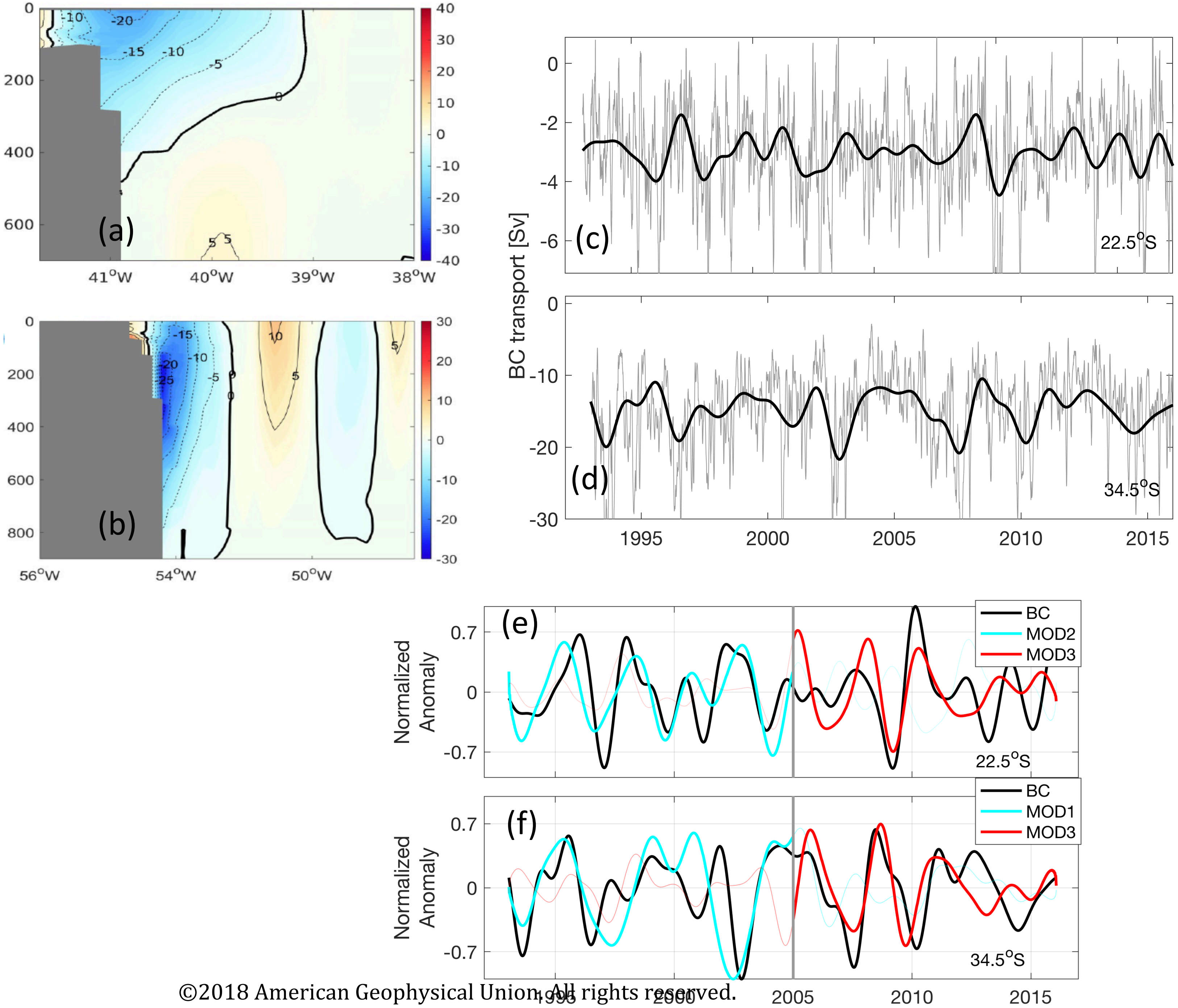
(a)
41°W
40°W
39°W
38°W
(b)
56°W
54°W
50°W
BC transport [Sv]
(c)
22.5°S
(d)
34.5°S
1995
2000
2005
2010
2015
(e)
Normalized Anomaly
BC
MOD2
MOD3
22.5°S
(f)
MOD1
34.5°S

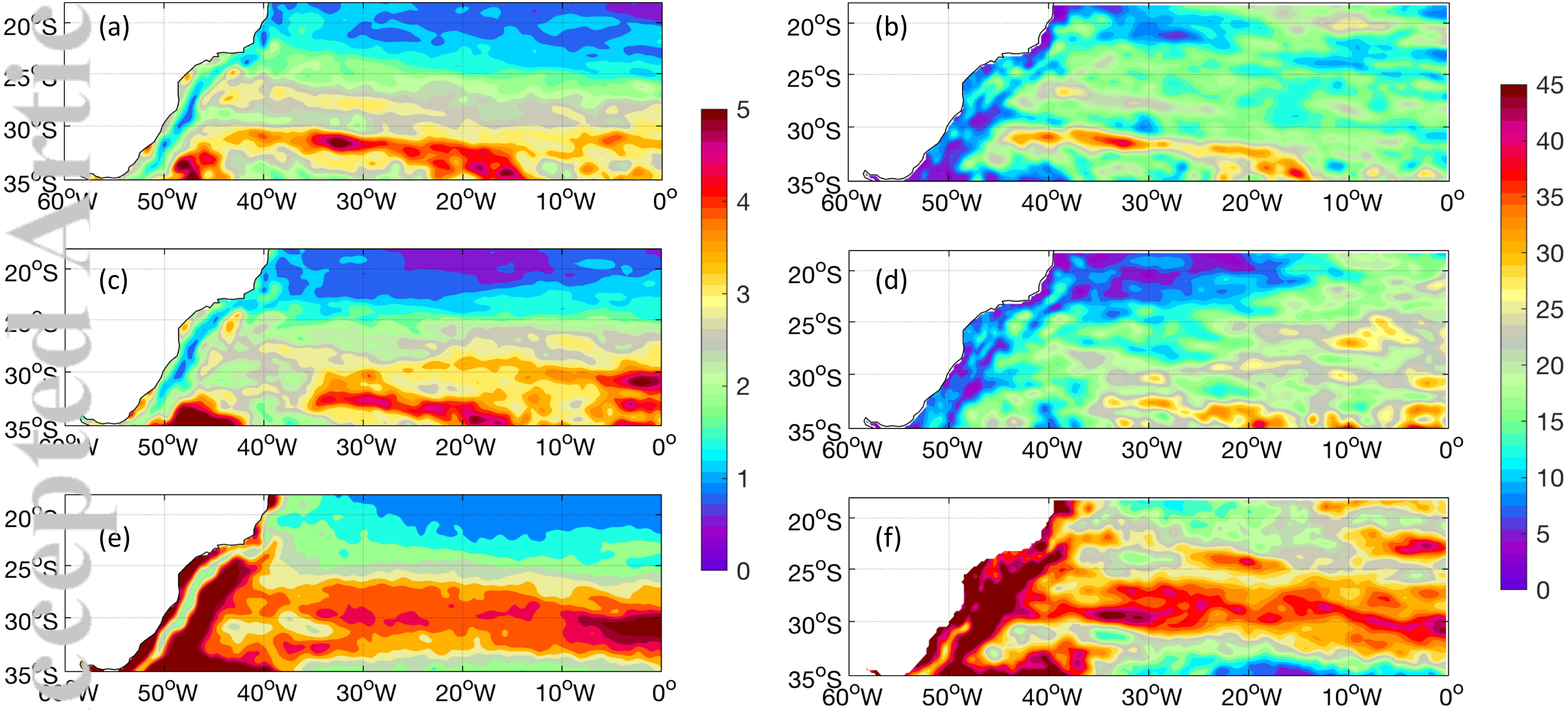

(a)
(b)
(c)
(d)
(e)
(f)
20°S
25°S
30°S
35°S
60°W
50°W
40°W
30°W
20°W
10°W
0°
0
1
2
3
4
5
0
5
10
15
20
25
30
35
40
45

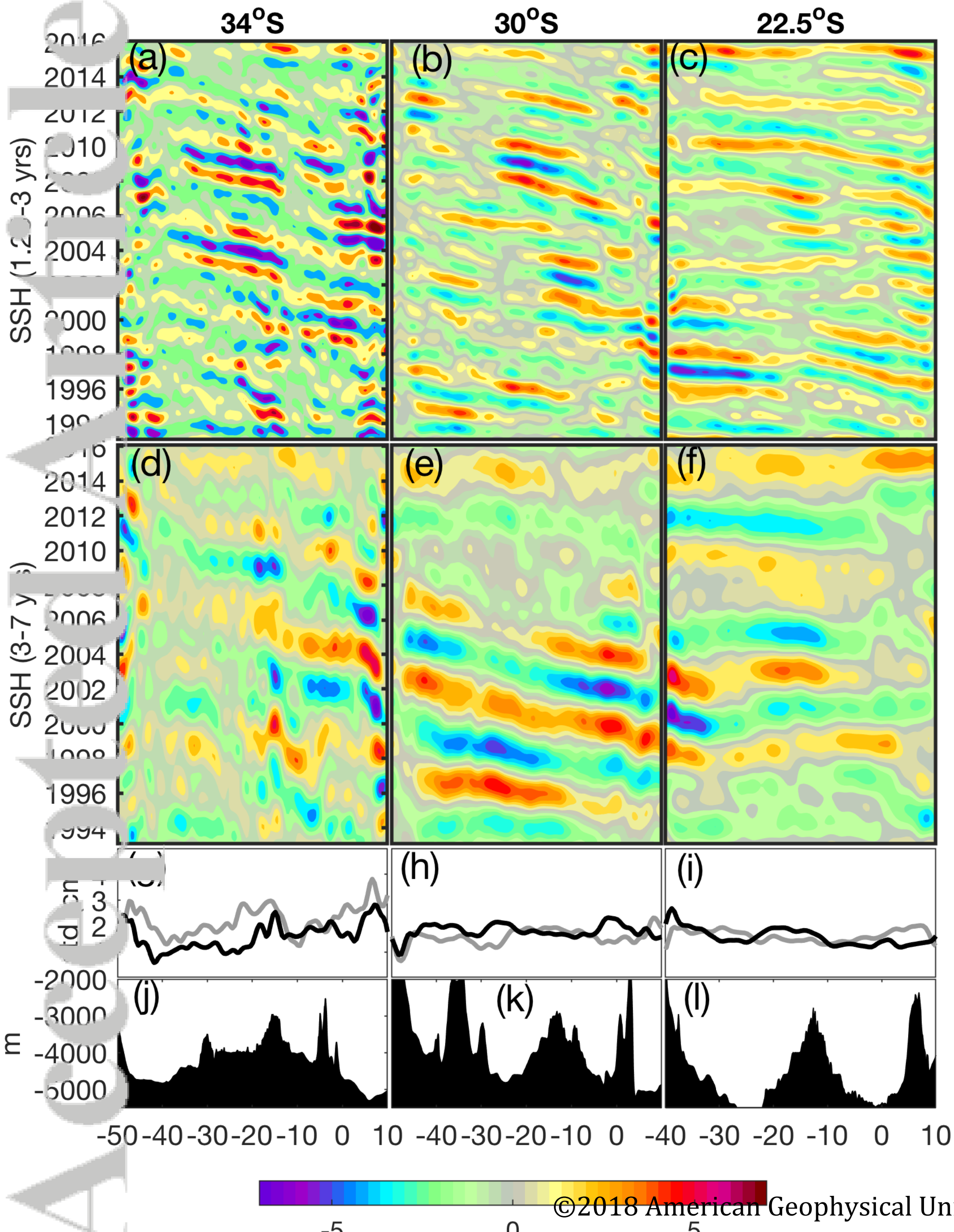

34°S
30°S
22.5°S
(a)
(b)
(c)
(d)
(e)
(f)
(h)
(i)
(j)
(k)
(l)
SSH (1.2-3 yrs)
SSH (3-7 yrs)
m
-2000
-3000
-4000
-5000
-50 -40 -30 -20 -10 0 10 -40 -30 -20 -10 0 -40 -30 -20 -10 0 10
-5
0
5

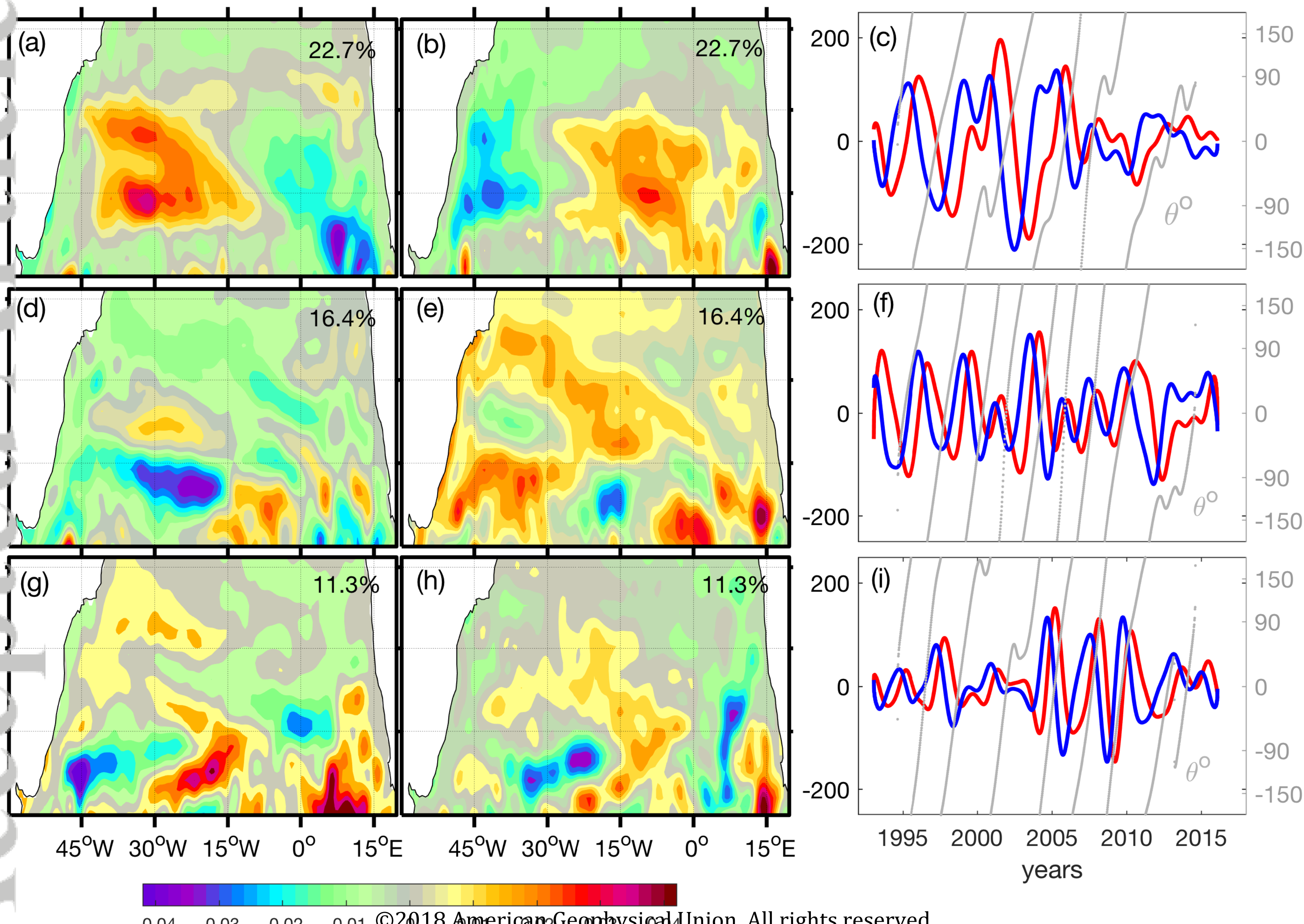

(a)
22.7%
(b)
22.7%
(c)
(d)
16.4%
(e)
16.4%
(f)
(g)
11.3%
(h)
11.3%
(i)
21°S
26°S
31°S
45°W
30°W
15°W
0°
15°E
200
0
-200
150
90
0
-90
-150
θ°
1995
2000
2005
2010
2015
years
-0.04
-0.03
-0.02
-0.01
0
0.01
0.02
0.03
0.04

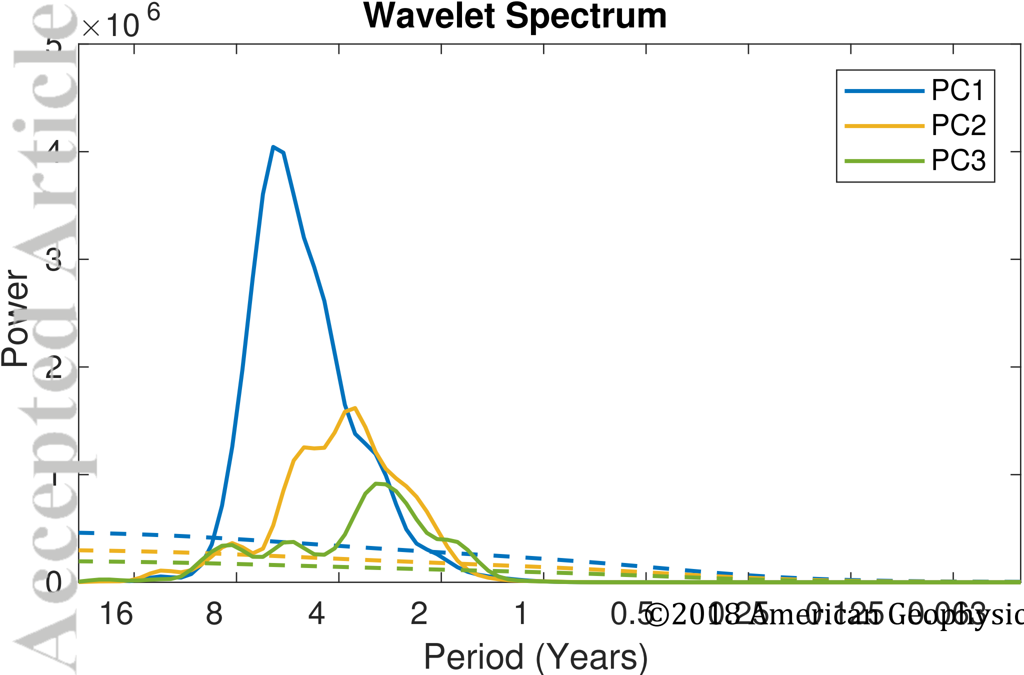
Wavelet Spectrum
×10^6
5
4
3
2
1
0
Power
PC1
PC2
PC3
16
8
4
2
1
0.5
0.25
0.125
0.063
Period (Years)

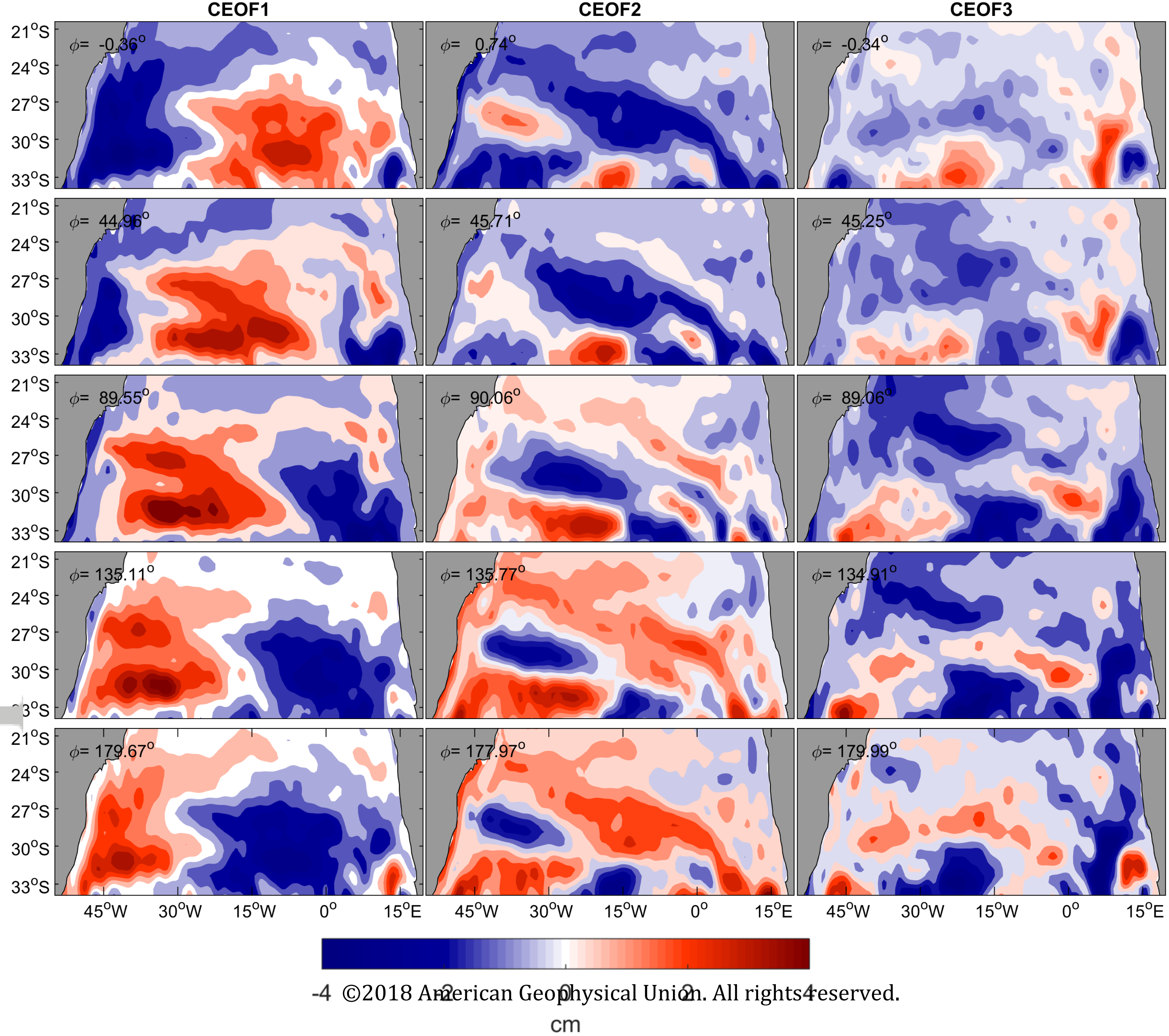
CEOF1
CEOF2
CEOF3
ϕ= -0.36°
ϕ= 0.74°
ϕ= -0.34°
ϕ= 44.96°
ϕ= 45.71°
ϕ= 45.25°
ϕ= 89.55°
ϕ= 90.06°
ϕ= 89.06°
ϕ= 135.11°
ϕ= 135.77°
ϕ= 134.91°
ϕ= 179.67°
ϕ= 177.97°
ϕ= 179.99°
21°S
24°S
27°S
30°S
33°S
45°W
30°W
15°W
0°
15°E
-4
-2
0
2
4
cm

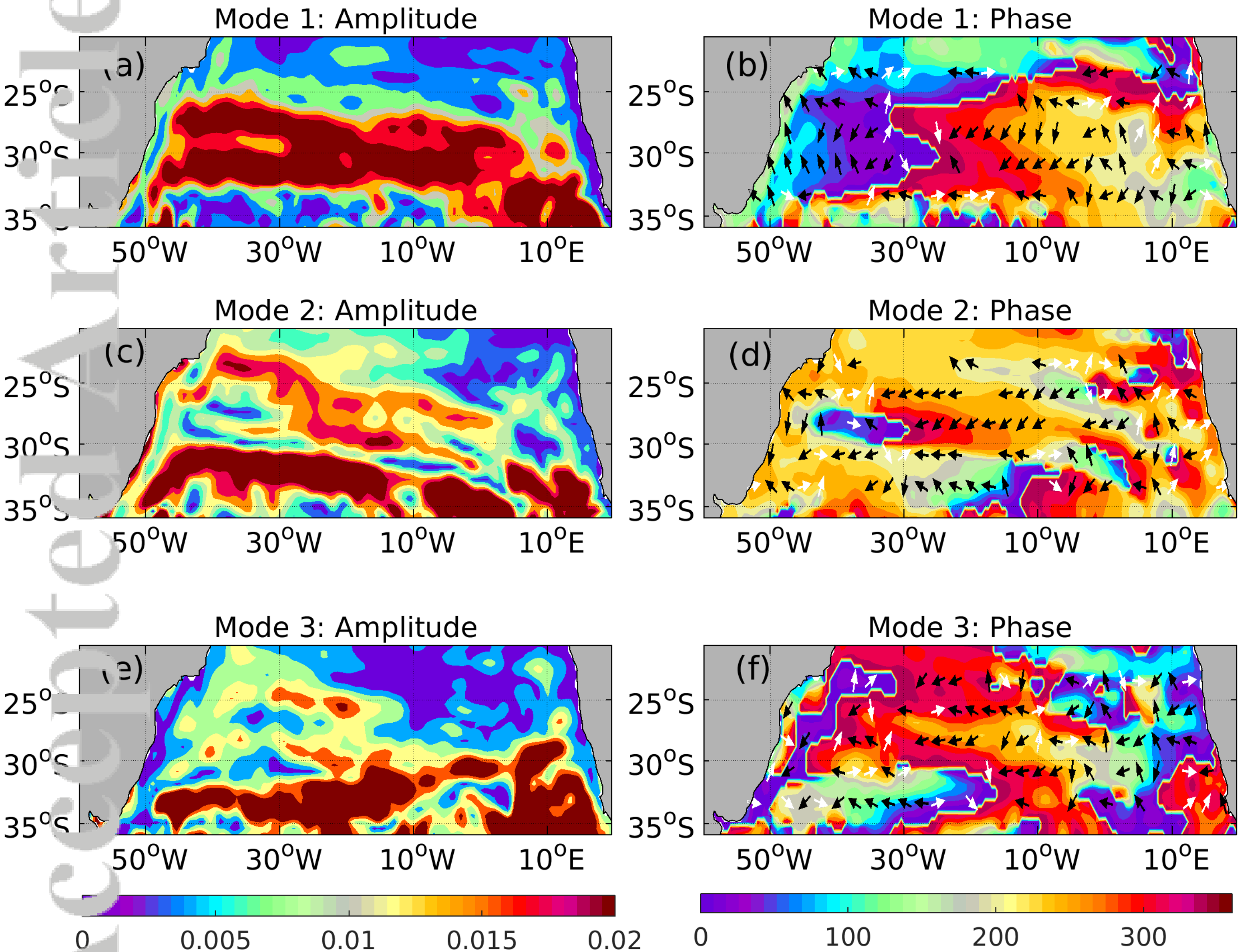

Mode 1: Amplitude
(a)
Mode 1: Phase
(b)
Mode 2: Amplitude
(c)
Mode 2: Phase
(d)
Mode 3: Amplitude
(e)
Mode 3: Phase
(f)
25°S
30°S
35°S
50°W
30°W
10°W
10°E
0
0.005
0.01
0.015
0.02
0
100
200
300

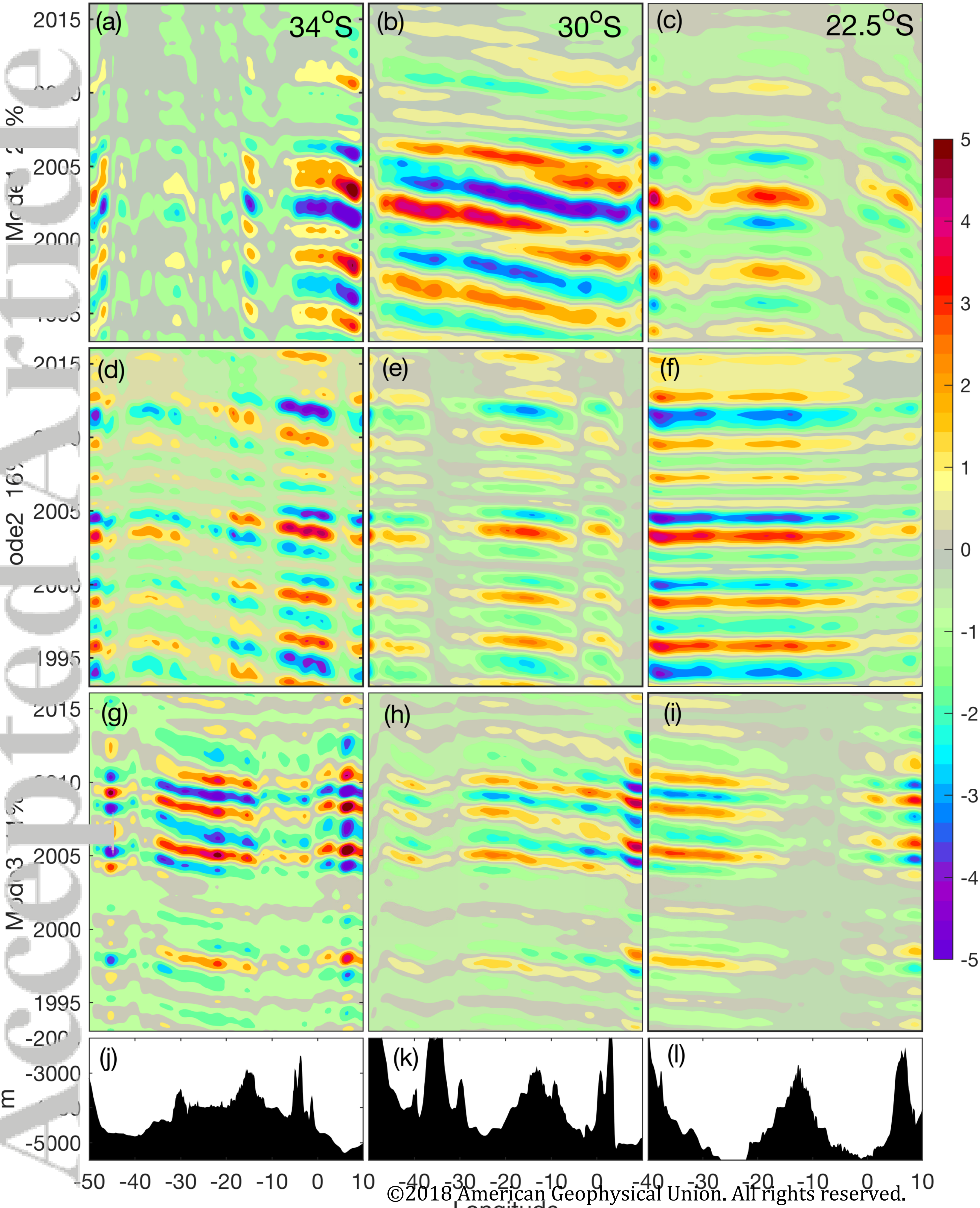

(a)
34°S
(b)
30°S
(c)
22.5°S
(d)
(e)
(f)
(g)
(h)
(i)
(j)
(k)
(l)
2015
2005
2000
1995
Mode2
Longitude
-3000
-5000
m
-50
-40
-30
-20
-10
0
10
5
4
3
2
1
0
-1
-2
-3
-4
-5

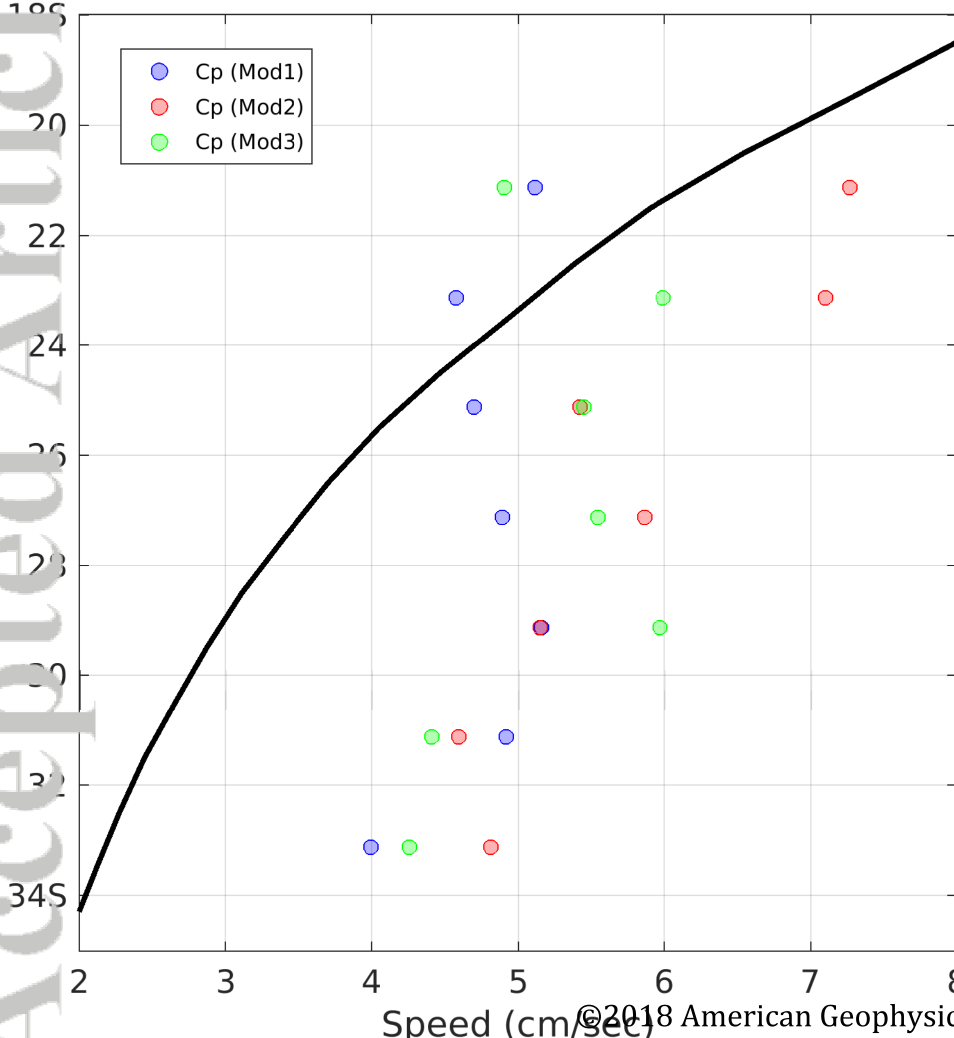
Cp (Mod1)
Cp (Mod2)
Cp (Mod3)
18S
20
22
24
26
28
30
32
34S
latitude
2
3
4
5
6
7
8
Speed (cm/sec)

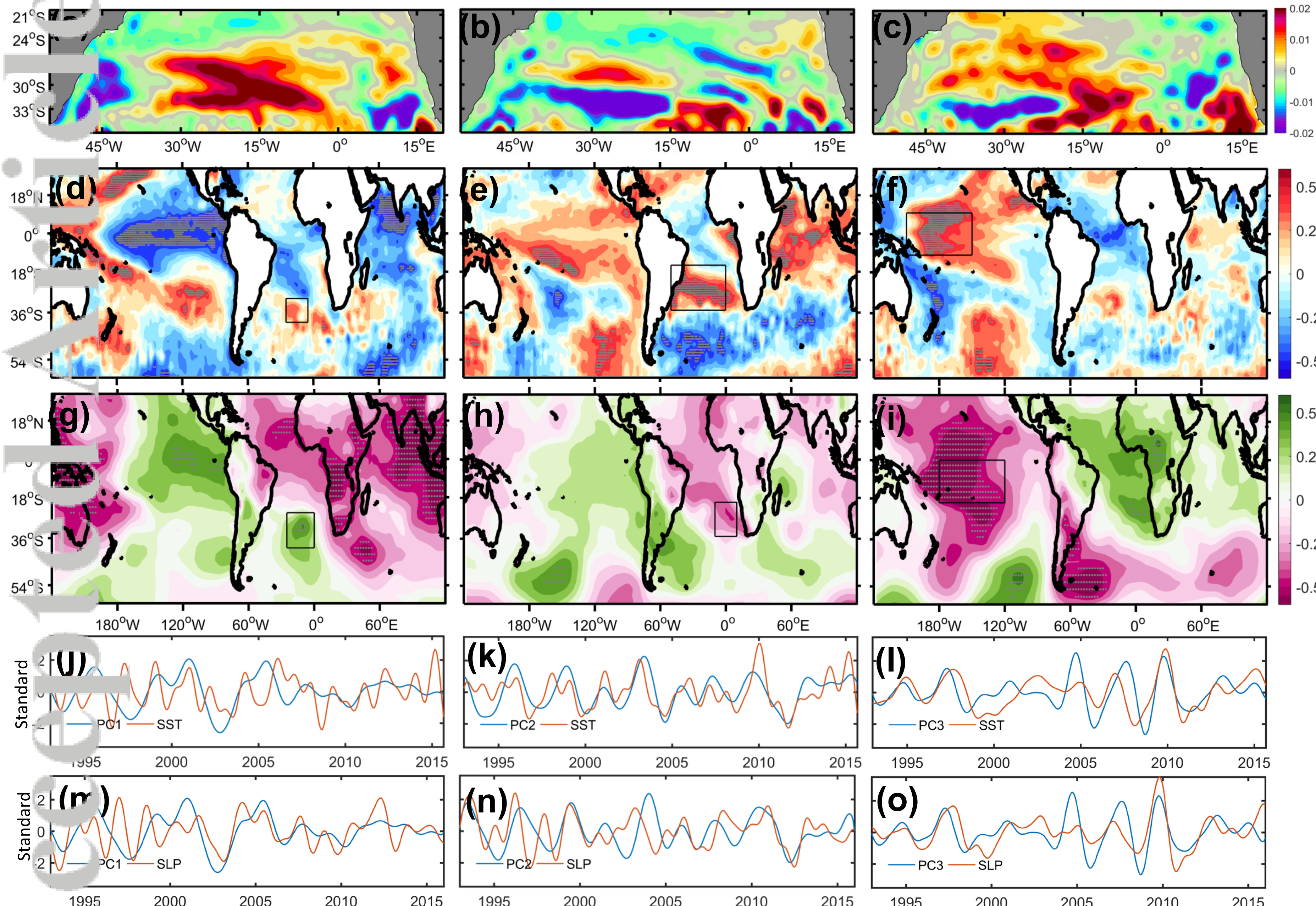

(a)
(b)
(c)
(d)
(e)
(f)
(g)
(h)
(i)
(j)
(k)
(l)
(m)
(n)
(o)
PC1
SST
PC2
SST
PC3
SST
PC1
SLP
PC2
SLP
PC3
SLP
Standard

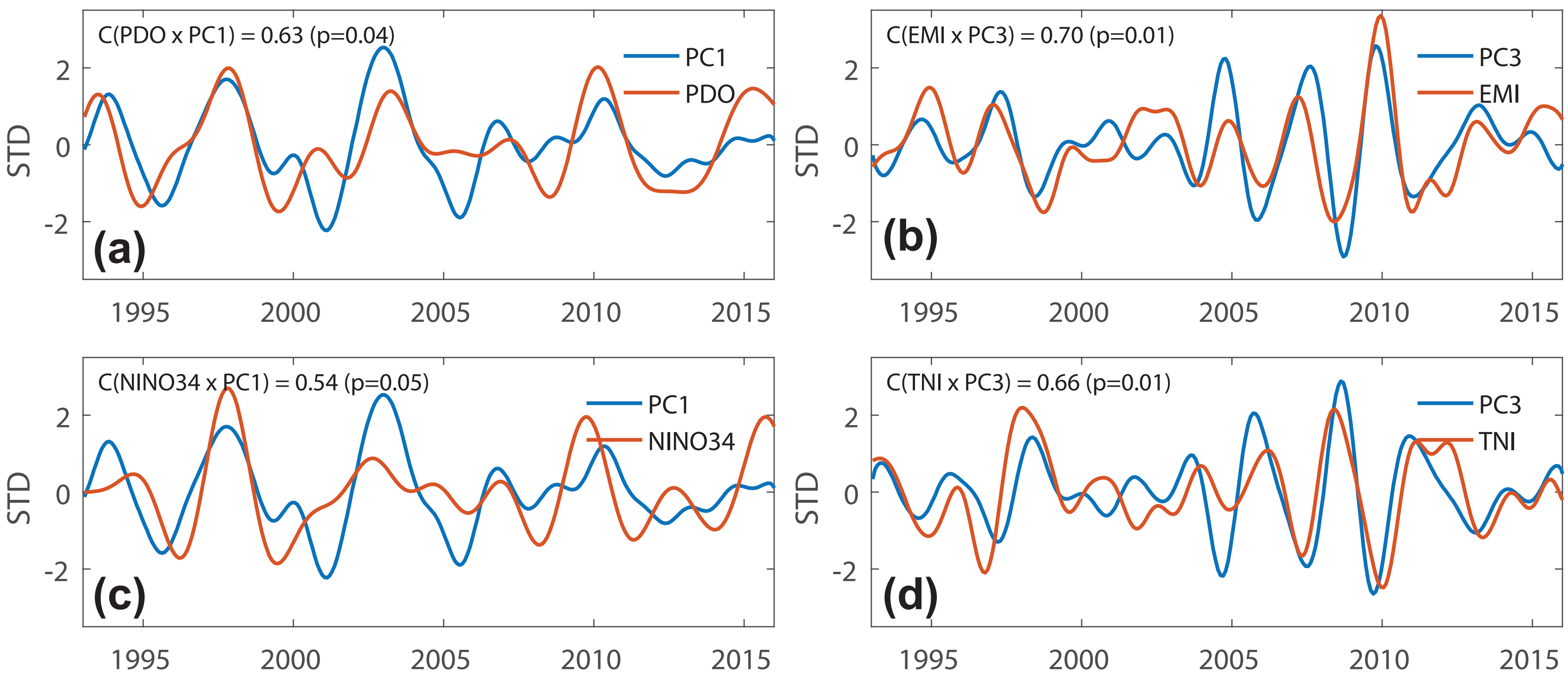

C(PDO x PC1) = 0.63 (p=0.04)
PC1
PDO
(a)
C(EMI x PC3) = 0.70 (p=0.01)
PC3
EMI
(b)
C(NINO34 x PC1) = 0.54 (p=0.05)
PC1
NINO34
(c)
C(TNI x PC3) = 0.66 (p=0.01)
PC3
TNI
(d)
STD
1995
2000
2005
2010
2015

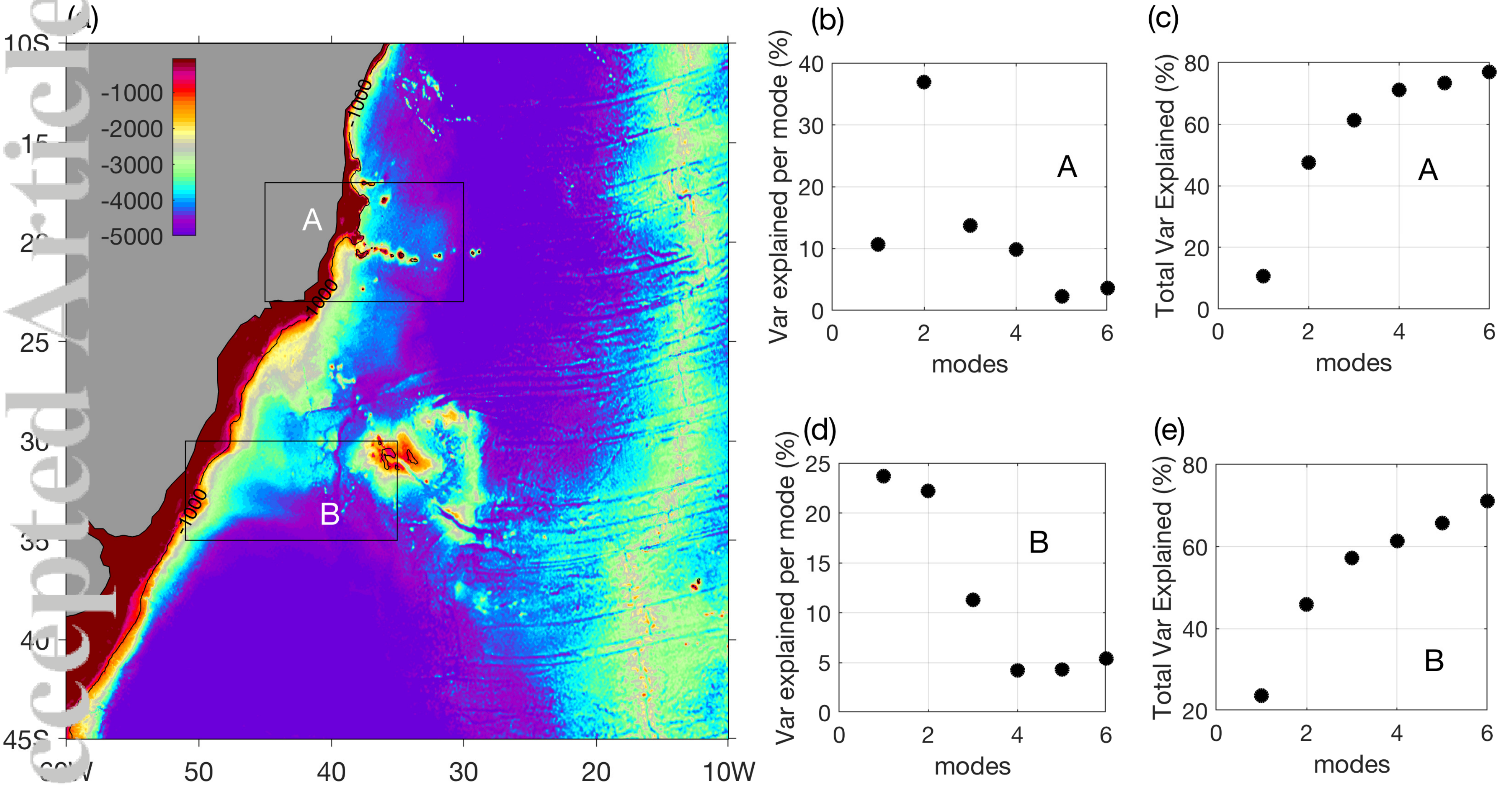

(a)
(b)
(c)
(d)
(e)
10S
15
20
25
30
35
40
45S
60W
50
40
30
20
10W
-1000
-2000
-3000
-4000
-5000
A
B
-1000
Var explained per mode (%)
Total Var Explained (%)
modes

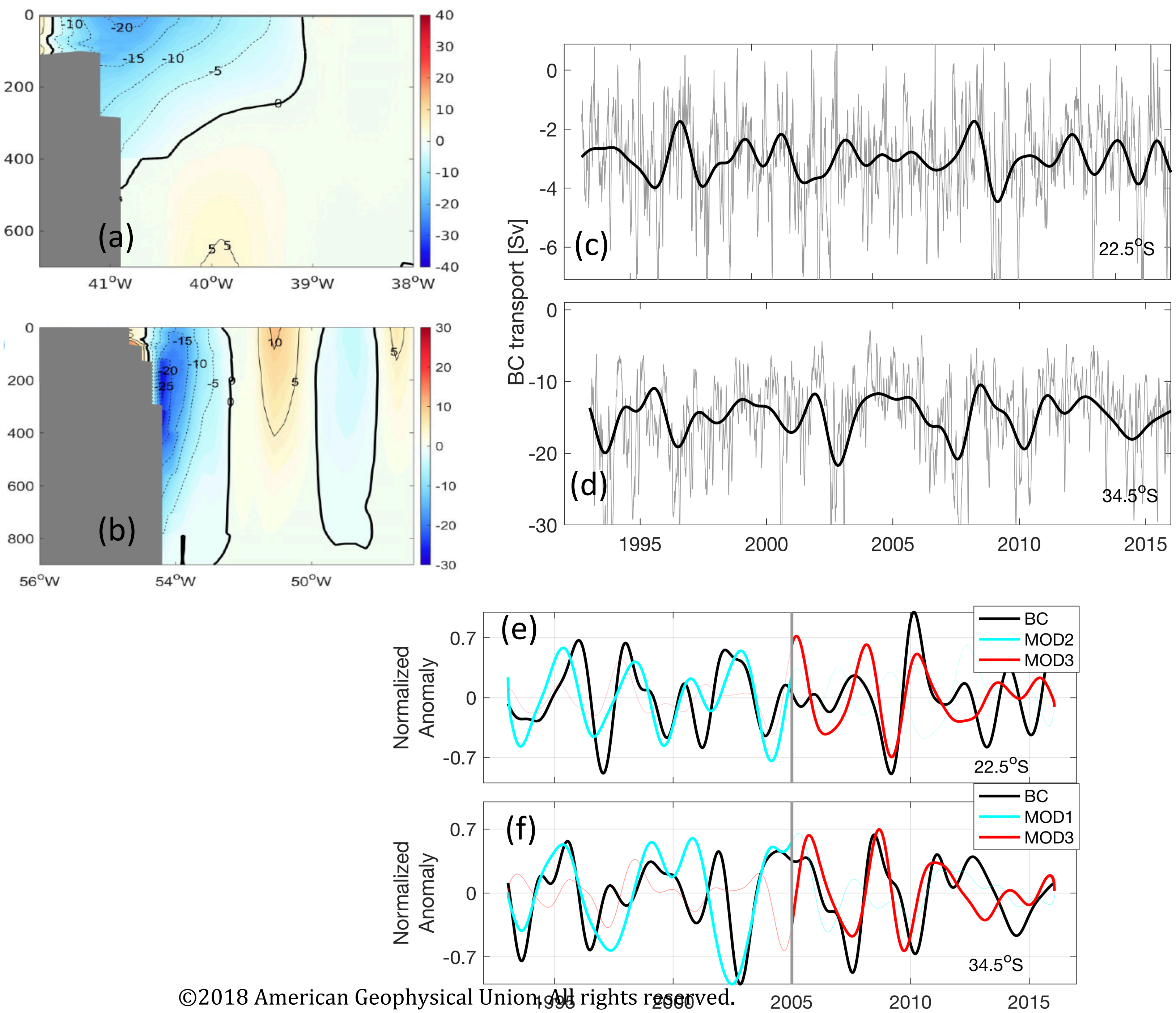

(a)
(b)
(c)
(d)
(e)
(f)
41°W
40°W
39°W
38°W
56°W
54°W
50°W
BC transport [Sv]
22.5°S
34.5°S
1995
2000
2005
2010
2015
Normalized Anomaly
BC
MOD2
MOD3
MOD1